Polar Science 30 (2021) 100700

Contents lists available at ScienceDirect

Polar Science

journal homepage: www.elsevier.com/locate/polar

Long-term changes in aerosol radiative properties over Ny-Ålesund: Results from Indian scientific expeditions to the Arctic

Mukunda M. Gogoi [a,*], Santosh K. Pandey [a], B.S. Arun [a,h], Vijayakumar S. Nair [a], Roseline C. Thakur [b], Jai Prakash Chaubey [c], Anoop Tiwari [d], M.R. Manoj [e], Sobhan Kumar Kompalli [a], Aditya Vaishya [f], S.S. Prijith [g], Prashant Hegde [a], S. Suresh Babu [a]

[a] Space Physics Laboratory, Vikram Sarabhai Space Centre, Thiruvananthapuram, India
[b] Institute for Atmospheric and Earth System Research, University of Helsinki, Finland
[c] Department of Physics and Atmospheric Sciences, Dalhousie University, Halifax, Canada
[d] National Centre for Polar and Ocean Research, Goa, India
[e] Divecha Centre for Climate Change, Indian Institute of Science, Bengaluru, India
[f] School of Arts and Sciences, And Global Centre for Environment and Energy, Ahmedabad University, Ahmedabad, India
[g] National Remote Sensing Centre, Indian Space Research Organization, Hyderabad, India
[h] Department of Physics, University of Kerala, Thiruvananthapuram, India

ARTICLE INFO

Keywords:
Black carbon
Aerosol scattering coefficient
Single scattering albedo
Aerosol size distribution
Aerosol chemical composition
Radiative forcing

ABSTRACT

Continuous long-term monitoring of black carbon (BC) mass concentration and aerosol light scattering coefficient (σ_{SCA}), supplemented by number size distribution and chemical composition, are utilized in this study to understand the temporal changes in aerosol properties, associated source processes and radiative effects at Ny-Ålesund (79 °N) in the Svalbard Archipelago. A statistically significant decreasing trend in BC (- 24.7 ng m^{-3} $decade^{-1}$) is observed during spring of 2010–2019. In contrast, σ_{SCA} depicted a general increasing trend (5.2 Mm^{-1} $decade^{-1}$) during 2011–2016. BC and σ_{SCA} were higher during winter and spring. Aerosol single scattering albedo was highest in May ~ 0.95 (during spring) and lowest in September ~ 0.87 (during summer). Fractional share of BC to total aerosol mass was higher in winter and summer. Anthropogenic SO_4^{2-} and NO_3^- (after $ssNa^+$) species dominated the summer, when total number and mass concentrations of aerosols were at their minimum. Elemental Carbon (EC) and Organic Carbon (OC) showed higher concentrations in spring with EC-to-OC ratio ~ 0.08 - 0.22. The columnar AOD varied between 0.01 and 0.20 (annual mean ~ 0.09), resulting in aerosol radiative forcing (in the top of the atmosphere) ~ 0.15 - 2.69 Wm^{-2} in the month of April (during spring). Potential source contribution function (PSCF) revealed the dominant source areas to be over Europe and Russia in terms of contributing to the seasonal high BC mass concentrations at Ny-Ålesund. Our study has also revealed an unusual impact of biomass burning aerosols (advected from the Alaska wildfire) during July 2015.

1. Introduction

Polar Regions are believed to provide an early signal of global warming and changes in the Earth's climate system, especially due to feedbacks associated with the high albedo of snow and ice (Shindell, 2008; Breider et al., 2017; IPCC 2018). Among the two Polar Regions, the Arctic is more sensitive to climate change, and observations over the past two decades have indicated that aerosols are one of the most influencing factors contributing to this (IPCC, 2013; Ren et al., 2020). In view of the significant rise in the ground and air temperatures over the Arctic at a comparatively higher rate than other regions of Earth, there have been concerted efforts towards better characterization of aerosol physico-chemical and optical properties and their radiative effects, relevant to Arctic (Gogoi et al., 2018 and references therein). In this regard, extensive studies have been made from distinct locations of the Arctic since the discovery of Arctic haze in the early sixties. Given the seasonality of Arctic haze and the associated transport of pollutants, several studies have focused on the Arctic winter and spring seasons (Radke et al., 1984; Shaw, 1995; Bodhaine et al., 1995; Sharma et al., 2004; Iziomon et al., 2006; Quinn et al., 2007; Garrett et al., 2011). On

* Corresponding author. Space Physics Laboratory, Vikram Sarabhai Space Centre, ISRO, Thiruvananthapuram, 695022, India.
E-mail address: dr_mukunda@vssc.gov.in (M.M. Gogoi).

https://doi.org/10.1016/j.polar.2021.100700
Received 14 November 2020; Received in revised form 10 May 2021; Accepted 19 May 2021
Available online 29 May 2021
1873-9652/© 2021 Elsevier B.V. and NIPR. This article is made available under the Elsevier license (http://www.elsevier.com/open-access/userlicense/1.0/).

the other hand, some other studies have focused on aerosol characterization in summer to understand distinct local source impact (e.g., Zhan et al., 2014), as during summer, the northward shifting of the polar front isolate the Arctic atmosphere from long-range transport from lower latitudes, especially at lower altitudes. Even though aerosol transported to the Arctic regions might have a larger influence on the Arctic climate than local pollution (i.e., aerosols generated within the Arctic circle, Shindell, 2007), understanding the role and occurrences of local surface pollution in the Arctic, which increases mainly during the summer, are important. Availability of solar radiation is another important aspect for conducting summer time studies to understand the impact of abundant natural sources of aerosols within the atmospheric boundary layer produced due to reduced ice cover and more ocean water (Ferek et al., 1995; Leck et al., 1996).

Despite the wealth of knowledge about Arctic aerosols, long-term observations of aerosol properties are crucial to infer the inter-annual variability as well as recent changes in local emission activities (such as increasing tourism and shipping emissions) that create spatial and vertical changes in aerosol distributions (Nagel et al., 1998; Flanner et al., 2007; Breider et al., 2017). Among the different types of aerosols, the climatic effects of Black Carbon (BC) over the Arctic is very important, as the surface albedo feedback caused by BC is often cited as the main contributor to the Arctic amplification. While aloft in the atmosphere, the cooling or warming effect of BC strongly depends on the albedo of the underlying surface and when deposited on to snow surfaces, BC reduces snow reflectance (Flanner et al., 2009). BC dry deposition (lesser over the polar regions) or wet deposition (more over the polar regions) can modify the emissivity by 0.4% in the global average (Jacobson, 2004), causing an average radiative forcing value of 0.10 W m^{-2} for the effects of BC on snow albedo (Hansen et al., 2000) and increase further to 0.15 W m^{-2} when BC is internally mixed with snow (Hansen and Nazarenko, 2004). Due to their relatively long lifetimes, BC is transported to polar regions (Stohl et al., 2006; Tomasi et al., 2007; Eleftheriadis et al., 2009; Chaubey et al., 2010), as well as to the high-altitude locations (Hyvärinen et al., 2009; Marinoni et al., 2010; Gogoi et al., 2014, 2021; Arun et al., 2019), which produces large uncertainties in assessing the radiative effects of BC at distinct regions of the globe. Among the two Polar Regions having extensive snow- and ice-coverages, the Arctic has more proximity to human activities and shipping emissions during summer, which results in the enhanced production of BC in the Arctic boundary layer (i.e., local contribution). Apart from BC, recent studies have shown the impact of long-range transport of sulfate aerosols from mid-latitude regions causing strong radiative imbalance in the Arctic (Ren et al., 2020), with anthropogenic sulfate contributing over 80% of total columnar anthropogenic aerosol optical depth (AOD) in April and May (Breider et al., 2014). Thus, it is imperative to understand the highly variable chemical composition, concentrations and the columnar abundance of aerosols over the Arctic those impart strong perturbation on the amount of energy passing through the atmosphere, thus influencing the radiative balance of the

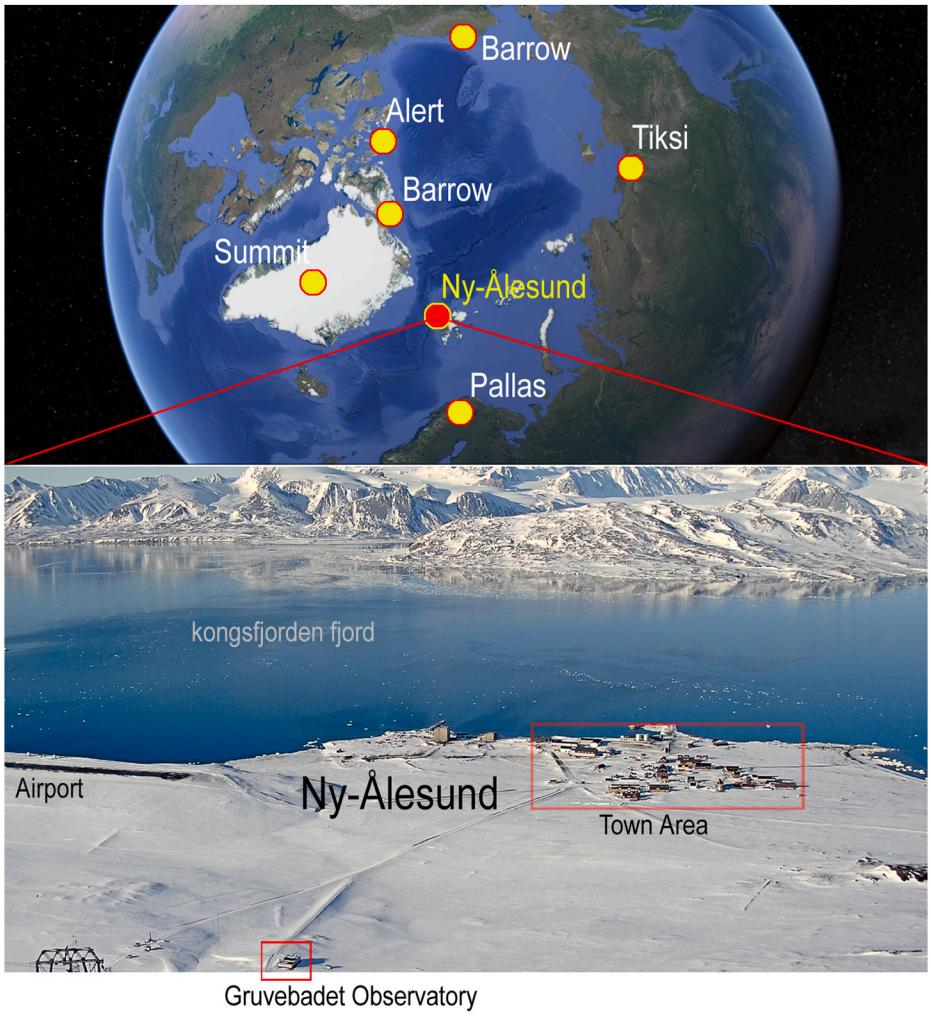


Fig. 1. (top) Location of Ny-Ålesund (78.9 °N, 11.8 °E) in the Svalbard archipelago of Norwegian Arctic; Positions of some other aerosol monitoring stations in the Arctic are also shown. (bottom) Gruvebadet (~10 m m.s.l.) observatory and village area at Ny-Ålesund (Image credit: Norwegian Polar Institute).

earth-atmosphere system.

Viewed against the above backdrop, we present the long-term characteristics of BC and light scattering coefficient, supplemented by size distribution and chemical composition of aerosols at Ny-Ålesund (79 ^{o}N) in the Svalbard Archipelago and infer the recent changes in the aerosol properties, associated source processes and radiative effects.

2. Sampling location, instruments, and database

In the top panel of Fig. 1, the geographic position of Ny-Ålesund (78.9 °N, 11.8 °E, 10 m m.s.l.) is shown. This is the northernmost research station near Kongsfjorden, surrounded by mountains and a tundra system (Pakszysand Zielinski, 2017). Like other experimentally focussed regions of Arctic, such as Alert (82.45 °N, 62.52 °W, 210 m m.s.l.) in Canadian Arctic, Barrow (71.32 °N, 156.6 °W, 11 m m.s.l.) in Alaskan Arctic, and Summit (78.36 °N, 38.5 °W, 3802 m m.s.l.) in Greenland, Ny-Ålesund is also relatively populated with more human activity during the summer period. To avoid the direct impact of the local emissions, measurements were carried out from Gruvebadet (~10 m m.s.l.), almost 1.5 km away from the Ny-Ålesund village. A view of the observational site is shown in the bottom panel of Fig. 1. The local activities (including transport) are minimal at Gruvebadet, with a few scientists visiting the station in a day.

Near real-time measurements of BC at Gruvebadet have been made using a multi-channel Aethalometer (Model: AE31, Magee Scientific Co., USA) at a time resolution of 30 min. The aethalometer measures the change in optical attenuation (ATN) of the light beam passing through a filter tape at seven wavelengths (370, 470, 520, 590, 660, 880, and 950 nm). The BC mass concentration is estimated from the change in attenuation at 880 nm, and the laboratory calibrated value of the specific mass absorption cross-section. Following the error budget described in several earlier papers, the maximum uncertainty in the measured BC is as high as 20%, with the higher percentage of error being applicable to lower concentrations (Gogoi et al., 2018). From the aethalometer measurements, aerosol absorption coefficients (σ_{ABS}) at different wavelengths (λ) are estimated incorporating the change in attenuation (ΔATN) of light due to aerosol load in the aethalometer filter media during sampling time 'Δt'. Further, linear relationships between σ_{ABS} and λ are utilized to estimate Ångstrom absorption exponent (α_{ABS}) for each set of aethalometer data.

Measurements of aerosol light scattering coefficients (σ_{SCA}) were made using a three-wavelength (450, 550, and 700 nm) Nephelometer (Model: 3563, TSI Inc.) at 5-min interval. Anderson et al. (1996) have reported an uncertainty of ±10% in measurement of σ_{SCA} by Nephelometer. The uncertainty arising out of the hygroscopic growth of aerosols due to differences in relative humidity (RH) between the ambient atmosphere and the detection area of in-situ measurements by nephelometer is also important. In the present study, the average RH inside the measurement chamber of Nephelometer was ~36.32% (N = 65267, standard deviation = ± 12.94, median = 33.8) with RH < 50% for more than 90% observations and RH < 60% for more than 95% of the observations. The ambient RH varied between 60% and 80%. Thus, the in-situ measurements of the light scattering properties of aerosols in the present study are representative of dry conditions, not affected by changes in ambient RH.

Based on the simultaneous measurements of σ_{SCA} and σ_{ABS}, aerosol single scattering albedo (SSA, ω) were estimated for each hourly data sets. For the estimation of instantaneous aerosol optical depth (AOD) from individual measurements of direct solar flux, a 5-channel handheld Microtops-II sun-photometer was used. Uncertainty in the measurement of AOD by Microtops II is ±0.01 (Morys et al., 2001). It is important to note that the Sun appears at this location during March (spring) and starts disappearing from October (autumn), making the measurements of AOD from the sunphotometer feasible between March to September months.

An Optical Particle Counter (OPC, Model No 1.108 of Grimm Aerosol Technik, GmbH, Germany), operated in count mode, provided aerosol number concentrations at 15 size channels in the diameter range between 0.3 and 20 μm. An averaging time of 1 min was used to obtain the number concentration. The instrument aspirated ambient air at a rate of 1.2 L per minute through an isokinetic inlet. In order to have suitable particle measurements by OPC under high RH conditions, specific weather protection housing was used. This housing contains an annular gap mixer by which particle-free dry air is re-fed to the sample air flow, which significantly decreases the relative humidity in the sample air stream. For generating particle free dry air from the exhaust of the spectrometer, a combination of silica-gel dryer and a filter was used. Thus, the particle measurements by OPC are relatively dryer than the ambient. Overall, an uncertainty of ±5% is expected in the number concentrations measured by the Grimm particle counter (Grimm user manual).

For chemical studies, aerosol samples were collected by operating high-volume air sampler for 16–24 h (the longer duration was chosen considering the very low aerosol concentrations at the site). The collected samples were analyzed for ionic and carbonaceous species for the representative months of spring (MAM) and summer (JJAS). Details about the chemical analysis of aerosol samples are described in section 4.4.

Apart from measuring the various parameters of aerosols, the radiometric measurements were made to estimate spectral albedo (i.e., the ratio of the reflected to the incoming flux) over the observational site by using a Fieldspec Pro spectroradiometer (ASD Inc., Boulder, USA). Based on the downward and upward looking measurements by alternately flipping the sensor 3-times, spectral albedo of the surface was estimated in wavelength range: 350–2500 nm. During each of the measurements, 25 individual spectrums were considered to estimate the average spectra. The white reference measurements were carried out in every 10 min interval to ensure optimal measurements of radiations by the spectroradiometer. The measurements were carried out during uniform illumination conditions of fully clear sky days, thus avoiding the errors produced by the time varying water vapor and partial cloud coverage. More details about the spectroradiometer operations and precautions taken during the field measurements of spectroradiometer are available in Gogoi et al. (2016).

Table 1 lists the instrumentation, measurements periods and uncertainty in the measurements of various parameters. BC mass concentrations are presented for the period from June 2010 to December 2019. Measurements of the scattering properties of aerosols are confined to the period from 2011 to 2016. AOD measurements are representatives of the clear sky periods of spring and summer during 2011–2017. Similarly, size distributions of aerosols are representative of the period from 2015 to 2016. The study of the chemical properties of aerosols are representative of some specific periods, supplementing the observed physical and optical properties of aerosols.

3. Meteorological parameters

For the study period, information on the daily mean local meteorological parameters such as temperature (T, °C), pressure (P, hPa), relative humidity (RH, %), wind speed (W_S, m s^{-1}), and wind direction (W_D, in degrees at 6 GMT) were obtained from the sensors installed at the height of 8 m in Ny Ålesund, operated and maintained by Norwegian meteorological office and data available through Eklima web portal (www.eklima.no). The temporal variations are shown in the different panels of Fig. 2 and the climatological monthly mean values for all the parameters during 2011–2019 are listed in Table 2.

Air temperature shows significant month to month variations with the temperature above 0 °C from June to September, and subzero temperature during the rest of the months, having lowest temperature (- 10 °C) in March and the highest (~ 6 °C) in July. Mean values of atmospheric pressure remained above 1000 hPa for all the months. RH generally varied between 60% and 80% throughout the year. Surface

Table 1
List of parameters measured, instrumentation and period of measurements.

Parameter measured	Instrument used	Model	Wavelengths	Uncertainty	Period
BC mass concentration	Aethalometer	AE31, Magee Scientific	370, 470, 520, 590, 660, 880, and 950 nm	±20%	2010 (Jul) – 2019 (Dec)
Total scattering and backscattering coefficient	Integrating Nephelometer	TSI-3563	450, 550, and 700 nm	±10%	2011 (Jun) – 2016 (Aug)
Number size distribution	Optical Particle Counter	Model No 1.108 Grimm Aerosol Technik	0.3–20 μm, 15 size channels	±5%	2015 (Oct) – 2016 (Dec)
Aerosol Optical Depth	Microtop Sunphotometer	Solar light co.	380, 440, 500, 675, 870, 936, 1020 nm	±0.01	2011–2017
Spectral SW radiation	Spectroradiometer	FieldSpec Pro	350–2500 nm	5%–12%	2017 (Apr)

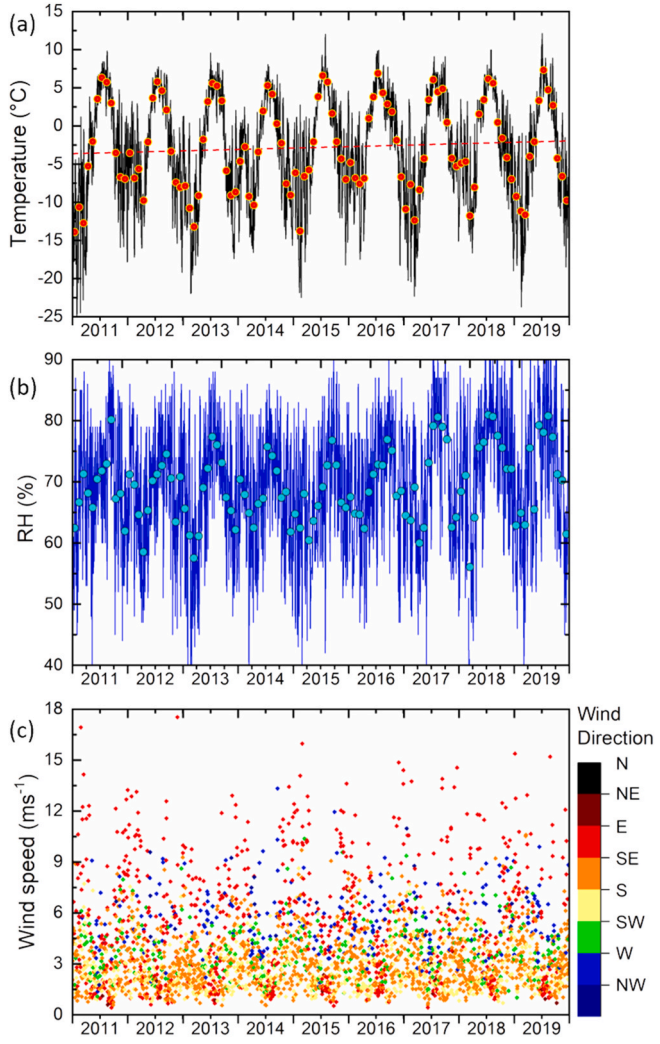


Fig. 2. Times series of the daily mean values of surface meteorological parameters, viz. (a) temperature (T), (b) relative humidity (RH), (c) wind speed (WS) and wind direction (WD) at Ny-Ålesund during 2011–2019. The red dashed line in the top panel is the linear regression fitted to the daily mean temperature data. The monthly mean values of T and RH are also shown (red and blue dots for T and RH respectively) along with the time series of daily mean values.

wind speeds remained more or less similar (~3–5 m s^{-1}) during all the months. Predominant wind direction is southeasterly to southerly, indicating winds from the clean, oceanic sectors to the observational site. Precipitation is higher during part of summer (JJAS), winter (DJF), and autumn (ON).

Table 2
Climatological monthly mean values of temperature (T), pressure (P), precipitation (PP), wind speed (WS), wind direction (WD), and relative humidity (RH) during 2011–2019.

Month	T (°C)	P (hPa)	PP (mm)	WS (m s^{-1})	WD (°)	RH (%)
Jan	−7.3 ± 3.4	1,006.8 ± 4.8	57.7 ± 65.2	4.46 ± 0.8	165.6 ± 15.0	66.9 ± 10.6
Feb	−8.3 ± 3.5	1,005.4 ± 6.7	50.4 ± 45.8	4.63 ± 0.5	168.5 ± 11.8	65.2 ± 10.4
Mar	−10.0 ± 2.8	1,004.4 ± 9.9	32.1 ± 28.1	4.55 ± 0.5	176.3 ± 15.5	64.6 ± 10.8
Apr	−7.5 ± 2.1	1,010.2 ± 5.5	19.9 ± 21.5	3.61 ± 0.7	179.7 ± 15.5	63.3 ± 10.4
May	−1.6 ± 1.8	1,014.9 ± 4.2	17.5 ± 12.6	3.50 ± 0.7	189.1 ± 6.7	67.2 ± 8.6
Jun	3.3 ± 0.5	1,011.9 ± 3.8	12.5 ± 15.3	3.13 ± 0.7	215.5 ± 7.5	71.6 ± 8.2
Jul	6.2 ± 0.6	1,011.8 ± 3.7	31.1 ± 33.5	2.87 ± 0.3	163.4 ± 11.5	74.8 ± 8.2
Aug	4.9 ± 0.6	1,009.4 ± 4.2	34.3 ± 31.5	2.99 ± 0.5	165.8 ± 16.7	75.7 ± 7.9
Sep	2.3 ± 1.4	1,008.1 ± 4.4	69.9 ± 47.5	3.42 ± 0.7	171.9 ± 16.4	76.3 ± 7.2
Oct	−2.2 ± 2.3	1,008.6 ± 4.4	49.9 ± 37.1	3.86 ± 0.8	177.0 ± 8.8	71.2 ± 9.4
Nov	−5.7 ± 2.2	1,005.9 ± 7.3	49.5 ± 49.7	4.77 ± 0.8	172.7 ± 14.8	66.7 ± 9.1
Dec	−7.6 ± 1.3	999.5 ± 6.6	37.2 ± 37.1	4.95 ± 0.6	176.3 ± 12.4	65.1 ± 9.8

4. Results and discussions

4.1. Seasonality and long-term trend in BC

The temporal variations of the daily and climatological monthly mean BC mass concentrations (M_{BC}) at Ny-Ålesund over a decadal period (from 2010 to 2019), along with the annual and diurnal cycles of BC (at different seasons) are shown in Fig. 3. The daily mean BC (Fig. 3a) varies over a wide range (between 4.78 ± 2.31 ng m^{-3} and 156.35 ± 25.90 ng m^{-3}) with~98% of BC < 100 ng m^{-3}. The climatological monthly mean BC (Fig. 3b) shows a systematic seasonality, with highest values (M_{BC} ~ 47.7 ± 36.32 ng m^{-3}) in March (spring) and lowest (M_{BC} ~ 22.52 ± 11.41 ng m^{-3}) in June (summer). M_{BC} remains lower in all the summer months and do not show significant month to month variability (seasonal mean ~ 24.95 ± 3.69). Despite large inter-annual variabilities in the monthly values of BC (Supplementary Figure – S1), a systematic seasonality with spring time high and summer low is indicative of the unique changes in (i) local and synoptic source impacts, (ii) influence of long-range transport, and (iii) removal mechanisms at different seasons.

Eleftheriadis et al. (2009) have shown a similar monthly pattern of BC at a high altitude station (474 m a.s.l.) in the Zeppelin mountain, located over the same study location. However, the annual mean BC at Gruvebadet (~30.37 ± 23.05 ng m^{-3}) during 2010–2019 (present study) is slightly lower than the annual mean BC at Zeppelin (~39 ng

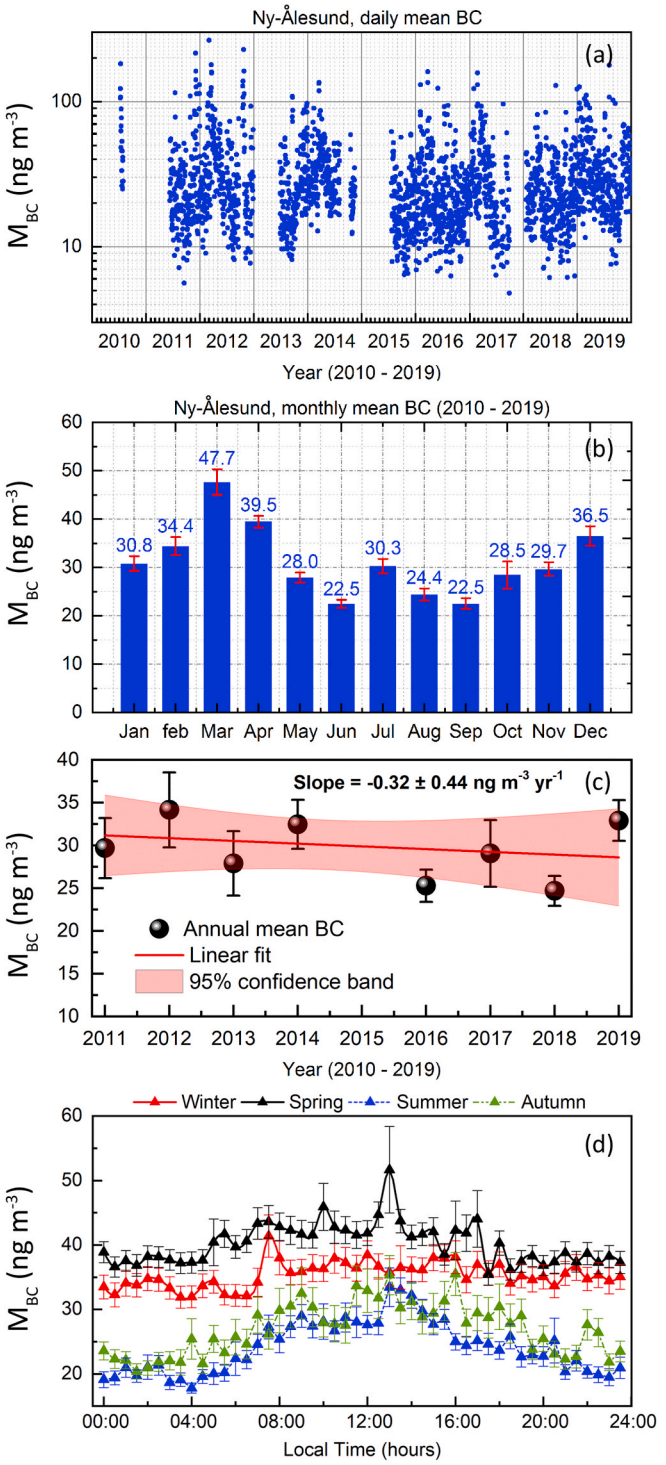


Fig. 3. (a) Time series of the daily mean values of BC mass concentrations during 2010–2019, (b) Climatological monthly variation of BC, (c) Annual variation of BC during 2011–2019, and (d) Diurnal variation of seasonal mean BC. The vertical bars indicate standard errors of the means.

m^{-3}) during 1998–2007. Interestingly, the seasonal amplitude of BC at Gruvebadet (BC_{spring}/BC_{summer} ~ 2) is much lower than those seen at Zeppelin (seasonal amplitude ~10; $BC_{Feb\text{-}Apr}$ ~ 68 ng m^{-3} and $BC_{Jun\text{-}Sep}$ ~ 7 ng m^{-3}). The observed seasonality of high BC at Gruvebadet and Zeppelin during spring could be attributed mainly to the synoptic influence. During winter, the southward expansion of the polar front (Barrie, 1986; Heidam et al., 2004) engulfs populated continents (North America, Canada, Eurasia, etc.), resulting in their impact in far remote northern locations due to emissions from these regions. This advection has different pathways to the Arctic region, which also forms a layered structure in the troposphere (Shaw, 1995; Warneke et al., 2009; Brock et al., 2011). During spring, as the temperature inversion moves up with the advent of the Sun, aerosols from the different regions of the troposphere get mixed up, resulting in the highest BC concentrations within ABL. Since Zeppelin is frequently representative of ABL conditions (Beine et al., 2001), apart from prevalent free-tropospheric conditions (Nyeki et al., 2005) at some part of the year, the distinct synoptic impact is effective at both Gruvebadet and Zeppelin. The polar front shrinks gradually during summer, excluding the populated continents (whichever engulfed in winter and spring). Thus, the virtual boundary between the Arctic and the populated regions modulated further by the increased scavenging of aerosols (both dry and wet, the effect of which vary with altitude), result in lower BC levels in the summer. However, relatively higher values of near-surface BC concentrations at Gruvebadet in summer with respect to that at Zeppelin can be connected to the increased local anthropogenic activity at Ny-Ålesund (Zhan and Gao, 2014). In addition to this, the scavenging efficiency of BC is also different at different altitude regions. The aged BC, coated by various soluble species, at higher altitudes, are less hydrophobic and more prone to nucleation scavenging by water drops, compared to the freshly emitted BC, whose scavenging efficiency is low due to their hydrophobic nature (Gogoi et al., 2016). Hegg et al. (2011) have also reported the varying nature of aerosol scavenging efficiency with altitude.

The annual mean values of BC (Fig. 3c) depict a general decreasing trend at an average rate of −3.2 ng m^{-3} decade^{-1}. This trend is estimated based on weighted least square linear regression method, where the fit is weighted by the annual variability (i.e., standard errors) giving lower weight to the highly variable data. To comply with this, we have excluded the annual mean BC of the year 2015, as there was data gap during Mar–May due to malfunction of the aethalometer. It is to be noted that, the estimation of BC trend from the annual mean values may not be the actual representation, as the monthly BC values at different years are highly random in nature (as shown in Fig. S1). Moreover, the lower magnitudes (<100 ng m^{-3}) and short observational period limit the accuracy of weighted trend estimates from the annual mean values. Given these limitations, we have estimated BC trends with respect to different seasons (supplementary Fig. S2) using the Sen's slope method and verified the significance of the trends using the Mann-Kendall test (details of the MK-test parameters are given in Table 3). From these, it is clear that the BC concentrations are decreasing irrespective of the seasons. But the observed trend (−24.7 ng m^{-3} decade^{-1}) is statistically significant only during spring ($p \sim 0.048$; $\alpha = 0.05$).

The above observations unambiguously support the long-term changes in the BC concentrations in the Arctic, but with varying magnitude at different seasons. The key factors those influence the long-term variability in BC at different seasons include: (i) large-scale circulation, (ii) pattern of precipitation, (iii) natural climate variability at annual to decadal time scales (Shen et al., 2017). Thus, the decreasing trend in BC during spring (an indication of the decreasing effect of Arctic haze, most pronounced in March/April period) could be attributed to the enhanced wet-scavenging of aerosols associated with the increasing warmer climate and resulting increased precipitation at higher latitudes. Since the concentrations of BC at Arctic mainly peak during the spring season (as shown in Fig. 3b), the decreasing-trend in BC during spring mainly controls the annual trend.

Several other studies have also reported decreasing trend in BC over the Arctic. BC at Zeppelin showed decreasing trend (- 9.5 ng m^{-3} decade^{-1}) during 1998 and 2010 (Eleftheriadis et al., 2009). Even though the BC concentrations at Gruvebadet is nearly 2–3 times higher (especially in summer) than the values at Zeppelin (Gogoi et al., 2016; Gilardoni et al., 2019), a similar trend in BC observed at both the sites are indicative of the effects of common sources influencing at different altitude regions of the atmosphere, though varying in magnitude.

Similar to Ny-Ålesund, a decline of about 55% BC concentrations at

Table 3
Mann-Kendall (MK) test parameters at different seasons, where N – total number of months w.r.t. different seasons.

Season	Start year	N (data)	sigma	Kendell's tau	p (2 tailed)	Z	Sen's slope
MAM	2012	18	26.40	−0.346	0.048	−1.969	−2.47
JJAS	2010	35	70.41	−0.156	0.191	−1.306	−0.47
ON	2011	16	22.21	−0.016	0.964	−0.045	−0.04
DJF	2011	19	28.58	−0.052	0.779	−0.279	−0.19
Annual	2010	88	277.46	−0.065	0.365	−0.904	−0.31

Alert is reported over a period of 13 years between 1989 and 2002 (Sharma et al., 2004). Breider et al. (2017) have also reported the decreasing trend of BC at Alert during 1989–2010 at an average rate of −16 ng m^{-3} $decade^{-1}$. Consistent with this, multidecadal observations of BC at several other regions of the Arctic have shown declining trend; viz. −9.0 ng m^{-3} $decade^{-1}$ at Barrow (in Alaska) during 1989–2010, and −45 ng m^{-3} $decade^{-1}$ at Kevo (in Finland) during 1980–2010 (Breider et al., 2017). Several aspects, such as a reduction in the emissions of fossil fuel BC and changes in the atmospheric circulation pathways, are concerned for the overall decline in BC concentrations at different geographic parts of the Arctic. For example, Sharma et al. (2004) have indicated the impact of a significant decline in the BC emissions from 1989 to 1998 at Ukraine, Belarus, Georgia, Armenia, Lithuania, Estonia, Latvia etc. on the observed BC trend at Alert. Similarly, strict mitigation policies those have been attempted and adapted since the 1990s in Europe (Sun et al., 2020) might have influenced the observed decreasing trend in BC at Ny-Ålesund. Global aerosol-climate model simulations of BC source apportionment over 16-source regions (between 66.5 and 90° N) of the Arctic depicted a decline of 23% surface BC concentrations in 2014–2018 relative to 1980–1984. This is attributed mainly to a reduction in emissions from Europe, Russia and local sources in the Arctic. Interestingly, positive trends in BC in the Arctic upper troposphere are attributed to the increases in emissions from South and East Asia (Ren et al., 2020).

Considering the short-term variability, BC at Ny-Ålesund shows (Fig. 3d) noon-time high, mainly during spring, summer, and autumn seasons. However, polar locations being possessed with very low BC concentrations and high solar elevation angles, large diurnal variations of BC are not expected, as seen at tropical locations. As the variations in solar elevation angles at the high latitudes are small, influences by thermal convection may have a minimal role in the vertical dispersion of the aerosols during the course of the day. Thus, the stable boundary layer prevailing most of the year (Stohl et al., 2006) at the Arctic prohibits the exchange of aerosols between the boundary layer and free-troposphere, resulting in an increase in the near-surface concentration associated with human activities (scientific as well as tourism) during sunlit periods. The build-up of aerosols in the ABL due to local activity is highest during summer (but most importantly remained below ~ 30 ng m^{-3}), which leads to maximum vertical heterogeneity during this period. The emissions from the tourist ships in summer significantly contribute to the elevated concentrations of total suspended particles (TSP), nss–SO_4^{2-}, organic carbon (OC), elemental carbon (EC), and trace elements (Mn, Fe, Co, Ni, As, and Se) in the ABL, while their concentrations reduce with altitude, as inferred from the measurements at Zeppelin (Zhan et al., 2014).

4.2. Scattering properties of aerosols

The time series of the daily mean values of aerosol scattering coefficients (σ_{SCA}) at three different wavelengths (450, 550, and 700 nm) are shown in Fig. 4a for the period 2011–2016. Despite the intermittent data gaps due to instrument failures, σ_{SCA} shows the broad seasonal features with daily mean values at 550 nm varying between 0.1 and 30 Mm^{-1} (with 94% of σ_{SCA} < 10 Mm^{-1} and 99.5% of σ_{SCA} < 20 Mm^{-1}; annual mean ~ 3.39 ± 3.64 Mm^{-1}). Interestingly, a statistically significant increasing trend (Table 4) in σ_{SCA} is seen with values (at 550 nm)

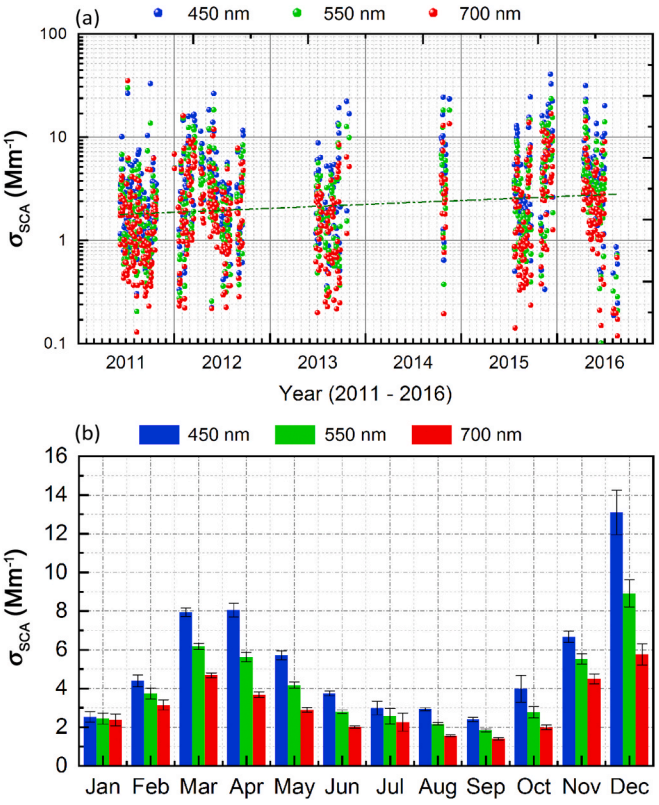


Fig. 4. (a) Time series of daily mean aerosol scattering coefficients (σ_{SCA}) at 450, 550, and 700 nm. The solid line through the points (550 nm) represents the linear least squares fit indicating the long-term trend in σ_{SCA}, its slope yielding the trend ($year^{-1}$). (b) Climatological monthly variation of σ_{SCA}. The vertical bars indicate standard errors of the means.

increasing at a rate of +5.2 Mm^{-1} $decade^{-1}$.

Examining the seasonal features of σ_{SCA} at Ny-Ålesund in Fig. 4b, it appears that the seasonal variations of σ_{SCA} at all the three wavelengths follow similar patterns, with higher values in March–May (~5.32 ± 1.03 Mm^{-1} at 550 nm) and December (~8.9 ± 0.7 Mm^{-1} at 500 nm), and lowest in September (~1.83 ± 0.07 Mm^{-1} at 550 nm). The seasonal variation of σ_{SCA} in our study is similar, though varying in magnitude, to several other sites throughout the Arctic, such as Alert, Barrow, Tiksi, and Zeppelin Mountain (Schmeisser et al., 2018), those are co-incident with Arctic haze phenomena (Shaw, 1995) resulting in enhanced scattering in the late winter and early spring. However, the seasonality in the present study is opposite to those seen at Pallas and Summit, which show maximum scattering coefficients in the summer and minimum in the winter. In terms of absolute magnitude, the annual mean value of σ_{SCA} in the present study (~4.06 ± 2.11 Mm^{-1} at 550 nm) is comparable to the values at Zeppelin (~4.35 Mm^{-1}; during 2010–2018); but lower than Tiksi (~12.47 Mm^{-1} during 2013–2018), and much higher than Summit (~1.74 Mm^{-1}; during 2011–2018). The scattering-coefficients at Summit is substantially lower due to the elevated position of the observational site (~3238 m m.s.l.), thus representing the characteristics of

Table 4
Detailed statistics of the trend in scattering coefficient.

Parameter	Start year	Base value (y-intercept at starting year)	Regression coefficient (R)	Slope (ω, year^{-1})	Standard deviation (σ_ω) of ω	$\lvert\omega/\sigma_\omega\rvert$	Trend (% year^{-1})
$\sigma_{SCA,\ 450\ nm}$	2011	3.42	0.392	0.837	0.196	4.26	22.44
$\sigma_{SCA,\ 550\ nm}$	2011	2.68	0.384	0.526	0.121	4.32	19.62
$\sigma_{SCA,\ 700\ nm}$	2011	2.11	0.339	0.286	0.069	4.15	13.57

free-tropospheric aerosols. In contrast, Tiksi is located near a populated area (~5 km outside the town of Tiksi) in northern Siberia, thus influenced by the local anthropogenic activities (e.g., energy production, transport etc.).

The observed spatio-temporal variability of σ_{SCA} in the Arctic is attributed to the seasonal and regional variations in the concentrations of transported sulfate aerosols as well as the sea salts produced regionally, which are the major scatterer of radiation over the Arctic (Barrie and Hoff, 1985; Quinn et al., 2007). While sulfate aerosol dominates the scattering during the haze periods (winter/spring), sea salt is the most important contributor in the summer time due to the melting of sea-ice and increase in open ocean conditions. While the sulfates keep the σ_{SCA} values higher during the spring, removal of the aerosols from the ambient during summer keeps the σ_{SCA} values lower in the absence of long-range transport.

In the context of long-term trend, the simulations of near-surface concentration and column burden of sulfate (which dominates light scattering, in general) also depicted a decreasing trend (20% per decade on the surface and 13% per decade in the column) in the Arctic during 1980–2018 (Ren et al., 2020). This is attributed mainly to the reductions in emissions from Europe and Russia. However, positive trends in sulfate and BC in the upper troposphere of the Arctic are depicted in their simulations due to increases in emissions from South and East Asia. On the other hand, time series analysis of CAMS (Copernicus Atmosphere Monitoring Service) model-based AODs simulated for Ny-Ålesund for the period from 2010 to 2015 has reported strong seasonal variation in AOD due to organic matter, dust, and sea-salt aerosols, in addition to that of sulfate (Pakszys and Zielinski, 2017). Viewed in this backdrop, increasing trend in σ_{SCA} seen in our present study is quite unique, which requires detailed investigation on the role of efficient light scattering by sea-salt aerosols delineating increasing trend in sea-ice melting associated with Arctic amplification. Accurate long-term quantification of the various factors responsible for enhanced light scattering is also important in the context of Arctic warming. Ren et al. (2020) have reported that sulfate-related Arctic warming is mainly due to the reduction in sulfate emissions at mid-latitudes and associated transport processes to the Arctic, which results in the enhancement of temperature gradient between the mid-latitudes and Arctic. This causes meridional heat transport, contributing to the warming of the Arctic.

In Fig. 5a, we examine the annual variation of aerosol single scattering albedo at 450, 550, and 700 nm. A clear seasonal transformation in SSA is seen with highest SSA in May ~0.95 (during spring) and lowest in September ~0.87 (during summer). The seasonal mean values are ~0.93 ± 0.05 and ~0.91 ± 0.07 during spring and summer respectively (all values are at 550 nm). Along with the seasonal change in the absolute magnitude of SSA, the spectral property of SSA also shows (Fig. 5b) distinct seasonal features, with relatively steeper spectra in spring (slope ~ −0.029) and autumn (slope ~ −0.047), indicating the dominance of fine mode aerosols. This is also supported by the steeper spectra of σ_{SCA} in winter (α_{SCA} ~ 1.47) and spring (α_{SCA} ~ 1.38) as compared to those during summer (α_{SCA} ~ 1.13) and autumn (α_{SCA} ~ 1.18).

A comparison of the values of SSA in the present study with those reported over several Arctic sites by Schmeisser et al. (2018) have revealed that the annual mean SSA at Ny-Ålesund (~0.92 ± 0.03 at 550 nm, present study) is comparable to the values at Zeppelin (annual mean ~ 0.945 at 550 nm during 2010–2018), even though SSA at Zeppelin do not show a distinguishable seasonality unlike the present study. Similarly, the annual mean SSA at Ny-Ålesund is comparable to the values at Alert but lower than Barrow (~0.96) and Tiksi (~0.934). Since a small change in SSA over highly reflective surfaces can change aerosol forcing from negative (cooling) to positive (warming), SSA is one of the most critical and uncertain aerosol parameters urging its accurate estimates over distinct snow-covered regions of the globe.

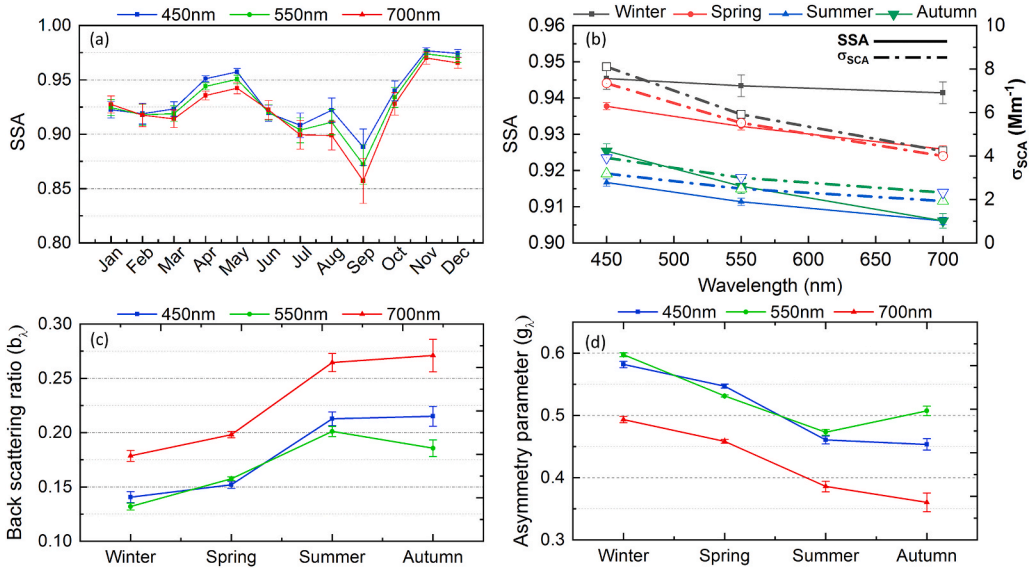


Fig. 5. (a) Annual variation of aerosol single scattering albedo (SSA) at 450, 550, and 700 nm. (b) Spectral variation of SSA (solid lines) and aerosol scattering coefficients (dashed lines) at different seasons; seasonal variation of aerosol (c) backscattering fraction and (d) asymmetry parameter at 450, 550, and 700 nm. The vertical bars indicate standard deviations of the means.

Similar to SSA, which depends strongly on aerosol size and chemistry, an accurate estimate of asymmetry parameter '*g*' is crucial, which represents the angular distribution of light scattering by an aerosol particle, with high values for large particles (indicating strong forward scattering). $g = -1$ indicates entirely backscattered, and $g = 1$ indicates entirely forward-scattered. In the present study, we have estimated the values of *g* using the backscatter fraction '*b*' (ratio of backscattering to total scattering coefficients) as described by Andrews et al. (2006). Fig. 5d shows the seasonal mean values of g, varying between 0.54 (during winter) and 0.38 (during summer) with an annual mean value of 0.52 ± 0.03. This is lower than the annual mean value at Zeppelin (~0.59, Schmeisser et al., 2018). As the values of g are indicative of the size distribution of aerosols, the lower values of *g* at Ny-Ålesund compared to that at Zeppelin are indicative of the relatively higher dominance of fine mode aerosols near the surface. Relatively lower values of aerosol backscattering fraction ($b < 0.2$; Fig. 5c) and higher values of asymmetry parameter (Fig. 5d) during winter and spring also supports that the synoptic-scale anthropogenic impact is dominant in winter and spring. In contrast, the natural sea-salt aerosols contribute to efficient light scattering in summer. On a seasonal scale, backscattering fraction varied between 0.13 (in winter) and 0.20 (in summer), while the seasonal mean values of asymmetry parameters are 0.59, 0.53, 0.47, and 0.51 (at 550 nm) during winter, spring, summer and autumn respectively.

To understand the relative impact of aerosol size and chemistry, we have further examined the association of scattering and absorbing aerosol index with aerosol extinction coefficients (Fig. 6). Scattering aerosol index (SAI) is determined as the product of α_{SCA} with σ_{SCA} whereas the absorbing aerosol index (AAI) is estimated as the product of absorption Angstrom exponent (α_{ABS}) with aerosol absorption coefficient (σ_{ABS}). As SAI carry the signatures of total particulate loading and the size distribution (Nair et al., 2020), a very good association ($R^2 > 0.8$) of aerosol extinction coefficients with SAI ($R^2 > 0.8$) during spring, summer and autumn indicate the dominant role of aerosol scattering on the light extinction properties. The highest slope is obtained during autumn, and least in winter, indicating the role of seasonal changes in aerosol size distribution on aerosol extinction properties. In contrast to this, extinction coefficients do not show strong association with AAI (indicating absorbing aerosols) except during spring ($R^2 \sim 0.61$). The slopes of the regression lines fitted between extinction coefficients and AAI also shows significant seasonal variability (slopes varying between 8.1 in summer and 24 in autumn). As AAI corresponds to biomass burning and fossil fuel combustions, the wide variability in the associations of extinction coefficients and AAI at different season is indicative of the impact of seasonally varying absorbing aerosol types on light extinction. Examination of the spectral properties of σ_{ABS} has revealed the signatures of absorbing aerosols from biomass burning sources in summer ($\alpha_{ABS} \sim 1.39$), while the rest of the period is mainly dominant of BC from fossil fuel combustion sources. This is indicated by the lower values of α_{ABS} in spring (~1.18), autumn (~1.05), and winter (~1.02). Even though the values of σ_{ABS} is lowest in summer, several recent studies have indicated the potential role of biomass burning aerosols on Arctic air pollution in summer (including Svalbard), despite the Arctic haze is the most dominant phenomenon in regards to the seasonality in the Arctic aerosols (Zielinski et al., 2020). A high level of BrC in biomass burning aerosols in the summer time can be a major climatic concern through atmospheric hearting as well as reducing snow albedo, as the solar radiations reach its maximum in summer. Breider et al. (2017) have also reported the presence of strong organic carbon (OC) content in Arctic summer due to emissions from boreal forest fires in peaking in July and August.

4.3. Aerosol size distribution

The aerosol number size distribution at different seasons in the size (diameter) range 0.3 and 20 μm (Fig. 7) reveals that fine particles having

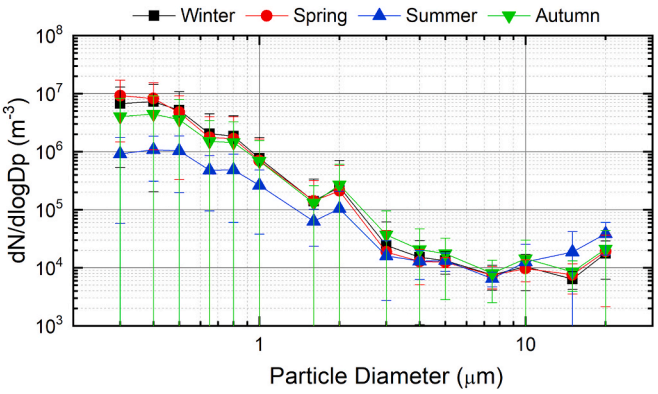


Fig. 7. Seasonal mean aerosol number size distributions in size range 0.3 μm and 20 μm, averaged for the data collected during 2015–2016.

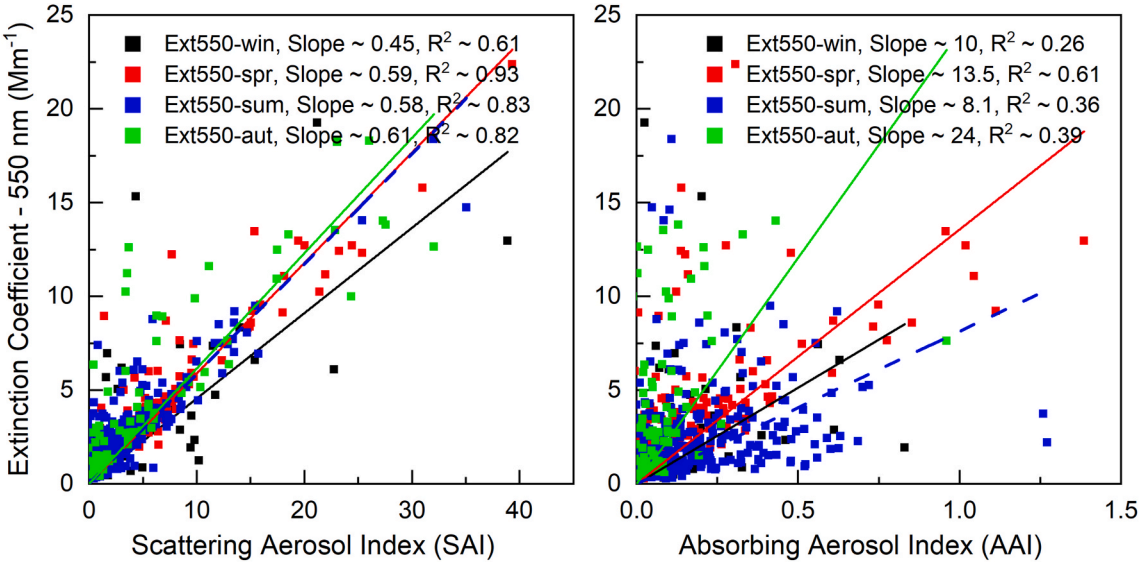


Fig. 6. Association of aerosol extinction coefficients with scattering aerosol index (SAI) and absorbing aerosol index (AAI) at different seasons.

diameter in the range of 0.3–1 μm mainly contribute to higher aerosol concentrations during winter, spring and autumn, while the relative contribution of coarse mode particles are dominant in summer. This is clearly depicted by the presence of particle concentrations in the size range >10 μm in summer. This observation supports the forgone observations those emerged from the optical properties of aerosols, such as higher values of backscattering fraction and lower asymmetry parameters in summer. During summer, the sea-salt particles of marine origin generated due to enhanced bubble breaking contribute significantly to the increase in coarse mode aerosol concentrations. Deshpande and Kamra (2014) have reported that the effect of winds from the oceanic sector is more effective in enhancing coarse mode particles in summer. Thinning of Arctic sea ice due to increasing temperature is a potential factor giving rise to ice fracturing and increased emissions of sea salt aerosol. Struthers et al. (2010) have reported that changes in the natural component (e.g., alteration of the sea-salt emissions due to reduced sea-ice extent) over the Arctic polar cap lead to the radiative imbalance of −0.2 Wm^{-2} to −0.4 Wm^{-2} for summer months. In contrast to this, the increase in accumulation mode particles is seen primarily in winter and spring. Based on aerodynamic particle sizer (0.5–20 μm) measurements during Apr–Sep 2013, Giardi et al. (2016) have also reported springtime enhancement in accumulation mode aerosols, mostly dominated by anthropogenic sulfate, at Ny-Ålesund. The increase in anthropogenic components in spring leads to the highest aerosols number concentrations.

The seasonal and monthly average values of aerosol total mass concentrations (M_T), along with the seasonal mean values of aerosol total number concentrations (N_T), are plotted in Fig-8a. The mass concentrations of aerosols are estimated from the number concentrations of aerosols (assuming aerosol density ~ 1 gm cm^{-3}) in distinct size bins between 0.3 and 20 μm. Further, the mass concentrations of PM1 (<1 μm), PM2.5 (<2.5 μm), and PM10 (<10 μm) particles are estimated in order to understand their fractional share to total aerosol load at different seasons. The seasonal characteristics of PM1, PM2.5 and PM10 are depicted in Fig. 8b, while the frequency counts of daily mean PM1, PM2.5 and PM10 are shown in Fig. 8c. Fig. 8d shows the fractional share of BC to total aerosol mass. The seasonal variations of M_T, PM1, PM2.5, and PM10 concentrations (as shown in Fig. 8a and 8b) show highest near-surface aerosol loading during spring (14.1 ± 17.2 μg m^{-3}), followed by autumn and winter and lowest in summer (7.2 ± 21.35 μg m^{-3}) having large day to day fluctuations in all the seasons. Interestingly, M_T shows large intra-seasonal variability, which leads to lowest seasonal mean M_T in summer, even though the monthly mean M_T is found to be highest in July during the period of observation. The significant reduction of M_T during August and September is mainly due to increased precipitation in these months (with peak in Sep ~ 69.9 mm; Table 2) as compared to that in July (~31.1 mm). Similar to M_T, N_T varies between the highest value in spring (~6.4 ± 5.1 cm^{-3}) and lowest in summer (0.82 ± 0.66 cm^{-3}). The summer values of N_T are approximately of the same order as those reported previously by Deshpande et al. (2014) for the period Aug–Sep 2007 (~0.84 particles cm^{-3}).

Examination of the percentage share of PM1 to total aerosol mass depicted very low values of PM1 fraction (~3.5% in winter and 1.4% in summer), indicating the pristine nature of the site with very less anthropogenic impact as compared to the very high values of accumulation fraction (>50% in general) those seen over many continental sites of the globe (e.g., Gogoi et al., 2011; Pillai et al., 2001). Interestingly, the percentage share of PM10 to total aerosol mass is >20%, having highest PM10 fraction in summer (~21.4%). This indicates abundant large-sized particles (>10 μm) at the observational site, which significantly contribute to the aerosol load near the surface.

Frequency of occurrences (Fig. 8c) of the daily mean values of aerosol mass concentrations in different particle size regimes indicates that more than 80% of the daily mean PM1 values were <0.2 μg m^{-3}, while > 75% of the daily mean PM10 values varied between 2 and 4 μg m^{-3}. On the other hand, PM2.5 showed a bimodal distribution with daily mean values peaking around 0.2 and 2 μg m^{-3}.

BC mass fraction (F_{BC}, as shown in Fig. 8d) follows nearly an opposite pattern to that of PM1. F_{BC} is higher in winter (~ 2.43) and summer (~ 2.15) than spring (~ 1.3). Despite such a lower contribution of BC to

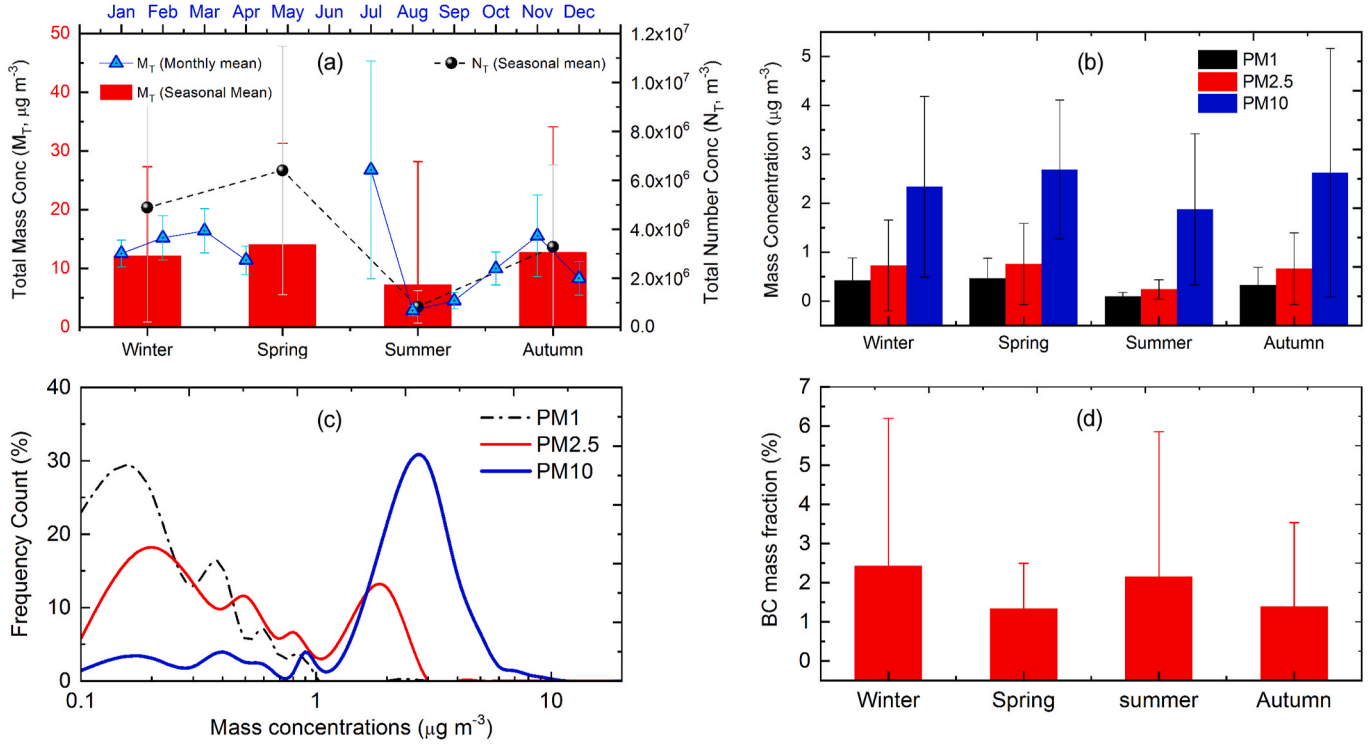


Fig. 8. Seasonal variation of (a) aerosol total mass concentrations (M_T) and total number concentrations (N_T), along with the monthly average values of M_T; (b) Mass concentrations of PM1, PM2.5 and PM10, (c) Frequency counts of the daily mean values of PM1, PM2.5, and PM10 and (d) seasonal average BC mass fraction.

total aerosol mass, the resulting SSA is ~ 0.91 ± 0.09 (at 550 nm) in summer, which can cause significant radiative impact above the highly reflective surface. The values of F_{BC} seen in the present study coincides with the values reported over the Canadian high Arctic. Results from airborne measurements at 60–6000 m altitude and based at four stations (Longyearbyen, Alert, Eureka, and Inuvik), Kodros et al. (2018) have reported size-resolved fraction of BC mass relative to total aerosol mass in the range of 1%–6%, contributing roughly 1%–5% to total aerosol optical extinction. Thus, accurate quantification of BC mass fraction to total aerosol mass over distinct snow-covered regions is essential as the regions with darker aerosol mixture lead to a larger positive radiative effect above the highly reflecting surface.

4.4. Chemical properties of aerosols

Apart from characterizing highly variable physical and optical properties of aerosols, understanding the chemical composition of aerosols is equally important to delineate the source and transport processes. Aerosol chemical composition is also important for evaluating sporadic pollution events as well as the factors affecting the long-term changes in the aerosol load and their climatic impact over a pristine region like Ny-Ålesund. In this study, the chemical properties of aerosols are examined in terms of major ionic species (cations and anions) during two representative months (Jul-2015 and Oct-2015) of summer and autumn. These two months differ considerably with respect to the prevailing local activities in the research village, Ny-Ålesund. The summer month (i.e., July 2015) also holds another special significance to study the chemistry of aerosols at Ny-Ålesund being influenced by an extreme wildfire event at Alaska. Several investigators have reported considerable impact of the fire not only on the chemistry of Arctic aerosols but also on the overall atmospheric dynamics, regional radiation budget and weather forecast (Lisok et al., 2018; Markowicz et al., 2016; Nikonovas et al., 2016; Ritter et al., 2018). Viewed against the above backdrop, the aerosol samples collected during July (representative of summer) and October (representative of autumn) of 2015 are analyzed. The extracts of the samples from filter punches were subsequently analyzed for major ions by a reagent-free ion chromatography (RF-IC) system (DX-2500 and ICS-2000, Dionex, USA), equipped with an automated Eluent Generator Module (EG50, Dionex, USA) and conductivity detector (CD25, Dionex, USA). The cations were separated on an IonPac CS17 (4 mm) column with methane sulfonic acid (MSA) as eluent, while the anions were separated on an IonPac AS11-HC (4 mm) column with potassium hydroxide (KOH) as eluent. The total mass of inorganic water-soluble ions (Na^+, NH_4^+, K^+, Ca^{2+}, Mg^{2+}, Cl^-, NO_3^- and SO_4^{2-}) was estimated, and their ionic concentrations were calculated based on the duration of the operating period and flow rate of filter samplings.

Further, to critically evaluate the sea salt, crustal and anthropogenic influence in the aerosols present during the two seasons of summer and autumn, we have calculated the concentration of some marker species, viz., sea-salt Sodium ($ssNa^+$), non-seasalt Calcium (nss-Ca^{2+}) and non-seasalt Sulfate (nss-SO_4^{2-}) based on the following equations (Virkula et al., 2006; Udisti et al., 2016):

$$ssNa^+ = (Rc.Na^+ - Ca^{2+})/(R_c - R_m) \quad (1)$$

$$nssSO_4^{2-} = (SO_4^{2-}) - 0.25 \times ssNa^+ \quad (2)$$

$$nssCa^{2+} = (Ca^{2+}) - 0.038 \times ssNa^+ \quad (3)$$

In the above equations, R_m and R_c are the mean ratios of Ca^{2+}/Na^+ in the marine aerosols and crust respectively. The values of R_m and R_c are assumed to be 0.038 (Nozaki, 1997) and 1.78 (Bowen, 1979). In equations (2) and (3), the numerical values 0.25 and 0.038 indicate the SO_4^{2-}/Na^+ and Ca^{2+}/Na^+ ratios (w/w) in sea-water respectively (Bowen, 1979). The sea-salt fraction of sulfate (ss-SO_4^{2-}) was calculated by multiplying the ss-Na^+ (as sea spray marker) concentration by 0.25. The crustal fraction of sulfate (cr-SO_4^{2-}) in the uppermost Earth crust was estimated by multiplying the nss-Ca^{2+} (as crustal marker) content by SO_4^{2-}/Ca^{2+} ratio (w/w) ~ 0.59 (Wagenbach et al., 1996).

The biogenic sulfate could not be calculated due to the non availability of the biogenic marker species, MSA. Assuming that biogenic sulfate in all seasons was less than the anthropogenic sulfate as also shown by the study of Udisti et al. (2016), we can state that even the subtraction of biogenic contribution (from the total sulfate (as per the equations mentioned in Udisti et al., 2016) would still yield a higher anthropogenic sulfate contribution in summer as compared to autumn, since the total sulfate, $nssSO_4^{2-}$ and $crSO_4^{2-}$ was almost 10 times higher in summer as compared to autumn in this study. The anthropogenic sulfate was estimated using the following eq.

$$An\text{-}SO_4^{2-} = nssSO_4^{2-} - crSO_4^{2-} \quad (4)$$

Fig. 9 (a and b) shows the concentrations of major ionic species in aerosols during the months of Jul-2015 and Oct-2015. The percentage contribution of each ion to total ionic concentration is shown in Fig. 9c, along with the sulfate source apportionment during Jul-2015 and Oct-2015. The concentrations of the cations and anions, representative of sea spray ($ssNa^+$, K^+, Mg^{2+} and Cl^-), crustal influence ($nssCa^{2+}$) and anthropogenic ($nssSO_4^{2-}$ and NO_3^-), are considerably higher in July as compared to October. This is also in line with the higher values of M_T in July as compared to that in October (Fig. 8a). The month of July is the peak of summer period with higher local emission sources from open water, frequent visits of tourist ships, open soil cover and tundra vegetation as compared to October when the local activities are at the minimum. Zhan et al. (2014) reports a two fold higher concentration of $nssSO_4^{2-}$ (~203 ng m^{-3}) than the median values of the entire sampling period of July 2012, when two cruise ships arrived at the coast of Ny-Ålesund.

Examining further the seasonal features, it appears that the concentration of all ions decrease from 100s of ng m^{-3} in July to 10s of ng m^{-3} in October. The observation of high BC concentration recorded in July as compared to October also shows that Ny-Ålesund in summer is highly influenced by pollution sources (as is indicated by higher BC mass fraction in Fig. 8). Irrespective of the inter seasonal variability of ionic concentrations, the $ssNa^+$ is the dominant ion during both July and October (Figs. 9a and 9b), contributing to 27% and 37%, respectively, in the total ionic concentration. The inter-ionic comparison within summer season indicates that anthropogenic species SO_4^{2-} and NO_3^- dominate (after $ssNa^+$). During autumn, SO_4^{2-} still continues to dominate the ion load (after $ssNa^+$) followed by Cl^- (Fig. 9b). As SO_4^{2-} in the aerosols could be derived from sea salt, biological and anthropogenic sources in the marine environment (Lefohn et al., 1999; Manktelow et al., 2007), we place our focus on sulfate aerosols, which are efficient scatterers of solar radiation leading to cooling of the earth-atmosphere system. Moreover, the indirect radiative forcing of sulfate aerosols is much more uncertain than their direct effect on radiation (Rongming et al., 2001). The study by Thakur and Thamban (2019) showed that gaseous SO_2 can be readily adsorbed on the surface snow in Ny-Ålesund affecting the acidity of snow. Thus knowledge of the sources and concentration of sulfate aerosols in fragile Arctic climate hold considerable importance.

Sulfate source apportionment shows that % contribution of ss-SO_4^{2-} and cr-SO_4^{2-} are higher as compared to the An-SO_4^{2-} during summer (Fig. 9c), emphasizing the important influence of the local sources at Ny-Ålesund. This is also noted in the % contribution of PM10 concentration to the total aerosol mass, which is much higher as compared to the PM1 or PM2.5 in the summer season. Thus, locally emitted coarse mode aerosols (basically from sea spray and crustal sources) play an important role during Arctic summer as it can alter the ionic budget, more specifically for Na^+ and SO_4^{2-}. During autumn, the relative contribution of An-SO_4^{2-} is higher (57%) as compared to ss-SO_4^{2-} and cr-SO_4^{2-} (Fig. 9c), despite low concentration of total SO_4^{2-} when comparing to the summer season. In July, the relative contribution of An-SO_4^{2-} to total SO_4^{2-} is just 26%, with a higher contribution of ss-SO_4^{2-} and cr-SO_4^{2-}, indicating the

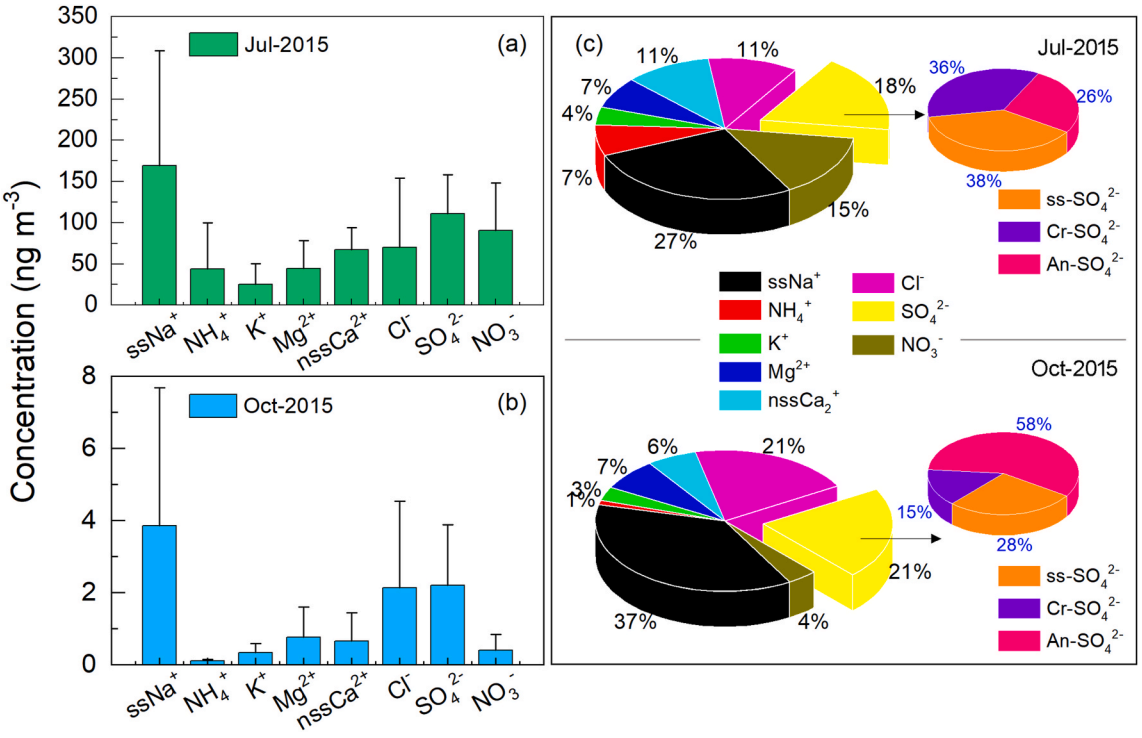


Fig. 9. Concentrations of major ionic species in aerosols during (a) Jul-2015 and (b) Oct-2015, representative of summer and autumn; The total number of samples considered for calculating the mean values are 15 (in July) and 4 (in October) respectively. (c) Percentage contribution of each ion to the total ion concentration in Jul-2015 and Oct-2015; along with the source apportionment of sulfate in the respective months.

impact of open fjord conditions and dust generated during the local activities in and around the Gruvebadet station during July. This observation suggests that summer aerosols at Ny-Ålesund indicate a mixed impact of local and long range transported pollution (Zhan et al., 2014). Apart from the effect of local sources, Ny-Ålesund during July-2015 was influenced by the air masses advected from Alsaska, experiencing the extreme fire events ever recorded. Unusually large wildfires in Alaska affected the region from mid-June to mid-July (https://fire.ak.blm.gov/). The smoke plume from Yukon-Koyukuk state, which was affected by 60 distinct wildfires, crossed the Arctic ocean and entered Ny-Ålesund on 9th July 2015 (Markowicz et al., 2016). During 10th-13th July, clear and continuous advection of air masses from Alaska to Ny-Ålesund is observed (Fig. 10a), leading to highest concentrations of NH_4^+, SO_4^{2-} and NO_3^- (Fig. 10b). The concentrations decreased progressively after 17th July 2015. These ions are mostly sourced from gas to particle conversion of the precursor gases like NH_3, H_2SO_4 and HNO_3 which are formed from the primary gas emissions (SO_2 and NO_x) during a forest fire (Bray et al., 2018; Behera and Balasubramanian, 2014). The air masses moved toward the coastline of Siberia after 13th July, stagnating there for a long time (Moroni et al., 2017). The concentrations of $nssSO_4^{2-}$ and NH_4^+ reported in this study for the July 2015 period are comparable to concentrations reported for the same period by Moroni et al. (2015).

Apart from the ionic species, we have examined the carbonaceous components: elemental carbon (EC) and organic carbon (OC), in total carbon in a representative month (April-2016) of spring as during this period the BC level peaks. The mass concentrations of EC and OC were estimated using an offline OC-EC analyzer (model 5L, Sunset Laboratory Inc., USA). The system works on the principle of the Thermo-optical transmittance (TOT) method following NIOSH (National Institute of Occupational Safety and Health) protocol. The analysis revealed a significantly higher amount of OC (344.1 ± 91.8 ng m^{-3}) and EC (55.2 ± 14.9 ng m^{-3}) concentrations with OC-to-EC ratio of ~6.73 (Fig. 11). The springtime OC in the present study is significantly higher than the summer time values (varying between 13.8 and 64.4 ng m^{-3}, with a mean value of 32.8 ng m^{-3}) reported by Zhan et al. (2014) over the same study location. Similalry, the EC-to-OC ratio also depicted much higher values in spring (~ 0.08 - 0.22) than summer (0.0076 - 0.028; Zhan et al., 2014). Several earlier studies have reported that, during spring, biomass burning aerosols contribute as high as 25% to total carbonaceous aerosols at Ny-Ålesund (Gogoi et al., 2016), as during this period the region is influenced by northward transport of agricultural burning and wild fires from Russia (Stohl et al., 2006). Accurate quantification of the radiative feedback processes associated with the large amount of OC, in addition to EC, is indispensable as the light-absorbing OC (i.e., BrC) is responsible for up to 50% of the total light absorption for biomass burning aerosols (Barrett and Sheesley, 2017 and references therein). On a global scale, the atmospheric burden of BrC is more than 3 times the BC burden, contributing up to 19% of the total absorption on Earth's radiation budget (Feng et al., 2013).

4.5. Aerosol optical depth and shortwave direct radiative forcing

Multi-year measurements of columnar aerosol optical depth (AOD) at 500 nm are shown in terms of daily and monthly mean values in Fig. 12a for the sunlit days of northern hemispheric spring and summer during 2011–2017. It can be seen that the daily mean values of AOD varied from a low value of ~ 0.01 (in July 2014) to as high as ~ 0.20 (in April 2017) with random day to day and intra-day variabilities. The mean AOD during the study period is ~ 0.09 ± 0.03 (at 500 nm). The AODs measured in this study are in line with the earlier measurements. Based on long-term AOD measurements at Ny-Ålesund during 1991–2010, and at several other Arctic sites during 1977–2010, Tomasi et al. (2012) have indicated that, climatologically, AODs (500 nm) greater than 0.1 persists during the spring, as against the occurrences of very low AODs during the summer. In contrast to this, the occasional higher values of AOD (>0.1 at 500 nm) seen during the summer in the present study might be associated with abundant coarse mode aerosols arising out of the open ocean conditions. The spectral variation of AOD also shows (Fig. 12b) relatively flatter spectra in summer with values of

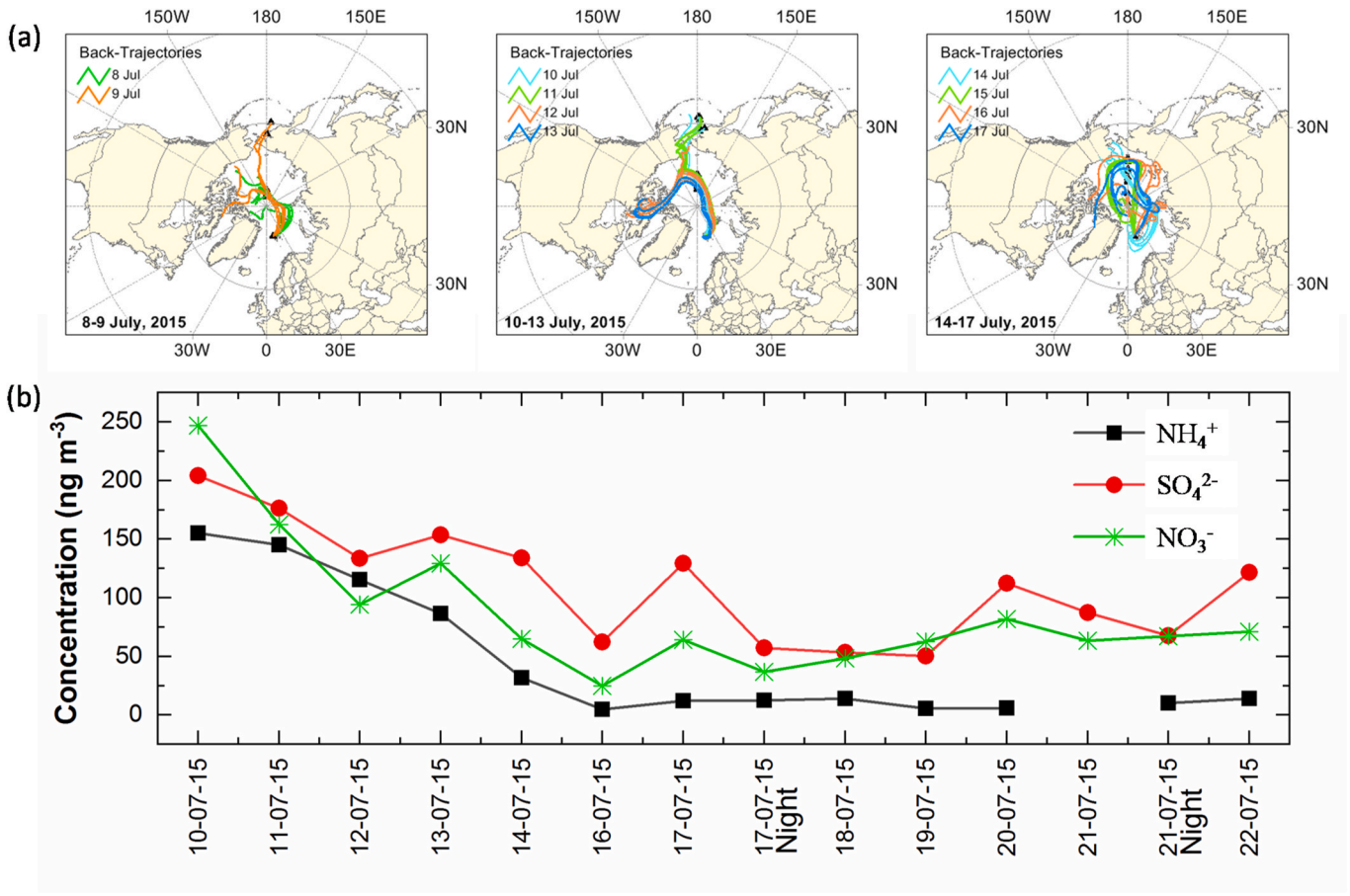


Fig. 10. (a) Isentropic 10-day airmass back trajectories ending at 500 m AGL over Ny-Ålesund during three different periods of Jul-2015. (b) The time series of the daily mean values (concentrations) of ionic species (e.g., NH_4^+, SO_4^{2-} and NO_3^-) during 10–22 Jul 2015.

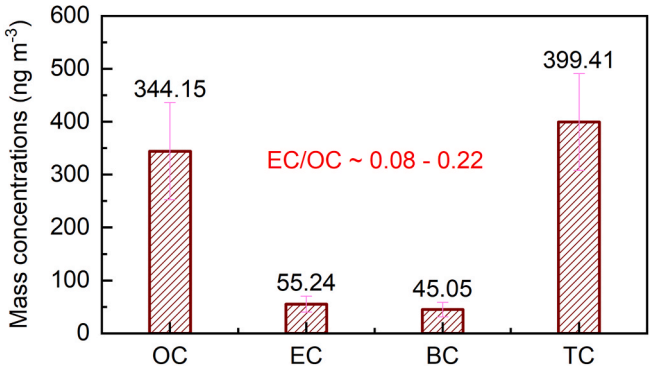


Fig. 11. Representative mass concentrations of carbonaceous aerosol species (OC, EC, BC, and TC) during the month of April-2016 (spring). A total number of 6-samples were considered for calculating the mean values of OC and EC.

Angstrom exponent as low as 0.6 (Fig. 12c) on some of the days. On the other hand, values of Angstrom exponents >1.0 for most of the days in spring. (see Fig. 13)

Examining AOD at different seasons, it appears that seasonal mean AOD in spring (0.11 ± 0.03) is slightly higher than the AOD in summer (0.09 ± 0.04). The high AODs are due to the winter-spring time Arctic haze, during which the weak scavenging mechanism is further conducive for maintaining a higher level of aerosol loading. The low AOD values during summer results from the reduced poleward transport of aerosols from the mid-latitudes, coupled with efficient dispersion of aerosols by wind and removal by precipitation.

To examine the direct radiative effect of aerosols over the highly reflective surface, the downward (incoming) and upward (reflected) radiations in the presence and absence of aerosols are simulated at each hourly interval (corresponding to different solar zenith angle) by using the Santa Barbara Discrete Ordinate Radiative Transfer (SBDART) model developed by Ricchiazzi et al. (1998) from which the daily (24-h) average values of aerosol direct radiative forcing (DRF) are estimated. The major input for simulating the radiations includes spectral (i) AOD, (ii) SSA, and (iii) asymmetry parameters (g); SSA and g at selected wavelengths were derived from the linear interpolation of the spectral values of σ_{SCA} and σ_{ABS} following Angstrom power law formula, i.e., $\sigma_{SCA,ABS} = \beta_{SCA,ABS}\lambda^{-\alpha_{SCA,ABS}}$, where $\alpha_{SCA,ABS}$ is scattering/ absorption Ångström exponent, and $\beta_{SCA,ABS}$ is constant. The spectral surface albedo in the shortwave regime 0.35–2.5 μm were obtained from spectroradiometer measurements over the study region. Profiles of all thermodynamic parameters, such as pressure (P), temperature (T) information are considered from the standard atmospheric model for Polar Regions, while that for Ozone concentrations (OMDOAO3e_003_ColumnAmountO3) were adopted from Ozone Monitoring Instrument (OMI) operating onboard Aura satellite and water vapor (AIRX3STD_006) from Atmospheric Infrared Sounder (AIRS) on Aqua satellite.

The estimation of aerosol direct radiative forcing (DRF) in the top of the atmosphere (DRF_{TOA}), surface (DRF_{SUR}), and atmosphere ($DRF_{ATM} = DRF_{TOA} - DRF_{SUR}$) yield surface forcing (cooling) in the range of −1.2 to −2.1 Wm^{-2}, with a corresponding TOA forcing of 0.15–2.69 Wm^{-2} during April. The clear sky SW DRF_{SUR} at Ny-Ålesund is lower than the regional averaged value (−4 Wm^{-2}) for the whole Arctic (north of 70°N) (Markowicz et al., 2021). With respect to region specific values, DRF_{SUR} at Ny-Ålesund during spring (present study) is lower than the average

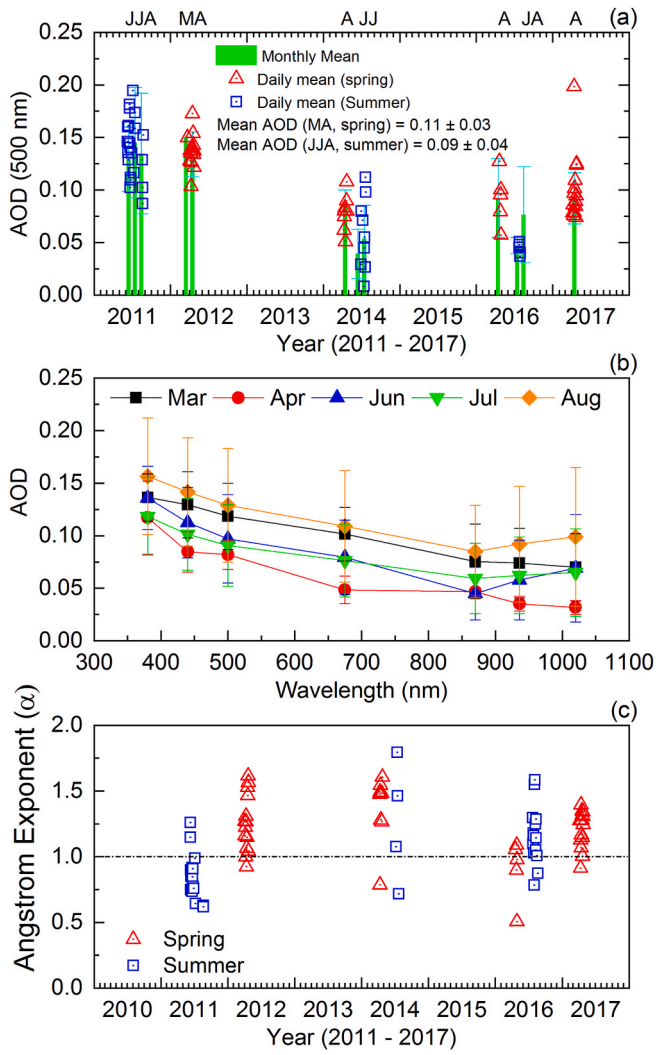


Fig. 12. (a) Daily (shown by the open squares and triangles) and monthly (shown by the histogram) mean values of aerosol optical depth (AOD) at 500 nm during the periods of spring and summer. The top-X axis labels denote the months by the first letter of each month. (b) Spectral variation of monthly mean AOD, where the vertical bars indicate the standard errors. (c) The temporal variations of the daily mean values of Angstrom exponent (open triangles are indicative of the daily mean values in spring, while the open squares are representative of the daily mean values in summer).

value (−10 Wm^{-2}) reported for the entire Svalbard region. The higher surface forcing at Svalbard region is attributed to the effect of sea salt aerosols, except summertime, as the region is surrounded by open water almost all year having enhanced production of sea salt (Markowicz et al., 2021). For the TOA, the forcing is dependent mostly on the surface albedo. Thus accurate information on spectral surface albedo is quite essential for the accurate estimation of DRF at the TOA over highly reflecting surface, whose properties changes significantly during different phases of snow melting.

4.6. Potential sources of BC

With a view to identifying the potential source areas affecting BC concentrations at Ny-Ålesund, we have adapted the potential source contribution function (PSCF) receptor model incorporating meteorological information in its analysis scheme. The PSCF technique for source identification is a conditional probability to identify specific upwind source areas contributing to the pollutant load above the threshold level at a receptor site. In the present study, we have utilized 10-years of isentropic airmass back trajectory data (obtained from the HYSPLIT model; Draxler and Hess, 1998) for running the PSCF model for different seasons. For this, the whole geographic region covered by the backward trajectories was divided into a gridded i by j array, and the PSCF for the ij^{th} cell is estimated as

$$PSCF_{ij} = \frac{m_{ij}}{n_{ij}} \quad (5)$$

Where n_{ij} is the total number of air masses falling into the ij^{th} cell during a season (irrespective of the years), and m_{ij} is the number of trajectory endpoints in the ij^{th} cell having corresponding measured pollutant concentration higher than the threshold value. The air parcel back-trajectories were calculated at a 1-h interval for a time period of 168 h (7-days) before arriving at 500 m above the receptor site (i.e., Ny-Ålesund). An angle distance algorithm was used to calculate optimum trajectory clusters.

Figure-13 shows the PSCF plots for BC mass concentrations corresponding to the seasonal data (irrespective of years) from 2010 to 2019. The annual mean BC of 30.37 ng m^{-3} is considered as a reference level for PSCF analysis. Both European (10°W-30°E) and Russian sectors (30–150°E) accounted for ~ 65% of trajectories in winter and spring with elevated PSCF in northeast Russia. During winter, the source regions expand far south towards the mid-latitude with several regions of elevated PSCF in the European and Russian sectors. North Europe is the dominant source region during summer, with ~27% of trajectories passing over it.

5. Summary and conclusion

We have examined the properties and long-term trends in the near-surface BC mass concentration and aerosol scattering coefficients, supplemented by size distribution and chemical properties of aerosols at Ny-Ålesund in Svalbard archipelago during 2010–2019. The main findings are listed below:

1. During the last decade (2010–2019), we observed a statistically significant decreasing trend in BC (−24.7 ng m^{-3} $decade^{-1}$) at Ny-Ålesund during the spring season, which is in line with the trend in BC reported over the same region during 1990–2009.
2. The light scattering coefficient of aerosols showed a weakly increasing trend (5.2 Mm^{-1} $decade^{-1}$) during 2011–2016, indicating the possible impact of decrease in sea-ice cover and increased contribution by sea-salt aerosols on enhanced light scattering.
3. Year-round monitoring of aerosol size distribution revealed the dominance of coarse mode aerosols in summer, with highest share of PM10 to total aerosol mass (~ 21.4%).
4. Aerosol total number and mass concentrations showed the lowest values in summer; however, BC mass fractions showed higher values in winter and summer. Significant intra-seasonal variability in aerosol mass concentrations leads to lowest seasonal mean values in summer. Near-surface aerosol mass concentration was highest in spring (~ 14 μg m^{-3}).
5. Among the ionic species, the $ssNa^{+}$ is the dominant ion during both summer and autumn, contributing 27% and 37% in the total ionic concentration respectively. On the other hand, the anthropogenic SO_4^{2-} and NO_3^{-} species dominate (after $ssNa^{+}$) the summer period. Considerable impact of Alaskan wildfires is also observed during July 2015, significantly enhancing the ionic concentrations in July as compared to October.
6. The EC-to-OC ratio varied between 0.08 and 0.22 during spring, which is significatnly higher than the EC-to-OC ratio in summer (~ 0.0076–0.028).
7. The average value of columnar AOD during the study period is ~ 0.09 ± 0.13 (at 500 nm). Aerosol direct radiative forcing during the sunlit periods of April (during spring) varied between −1.2 and −2.1

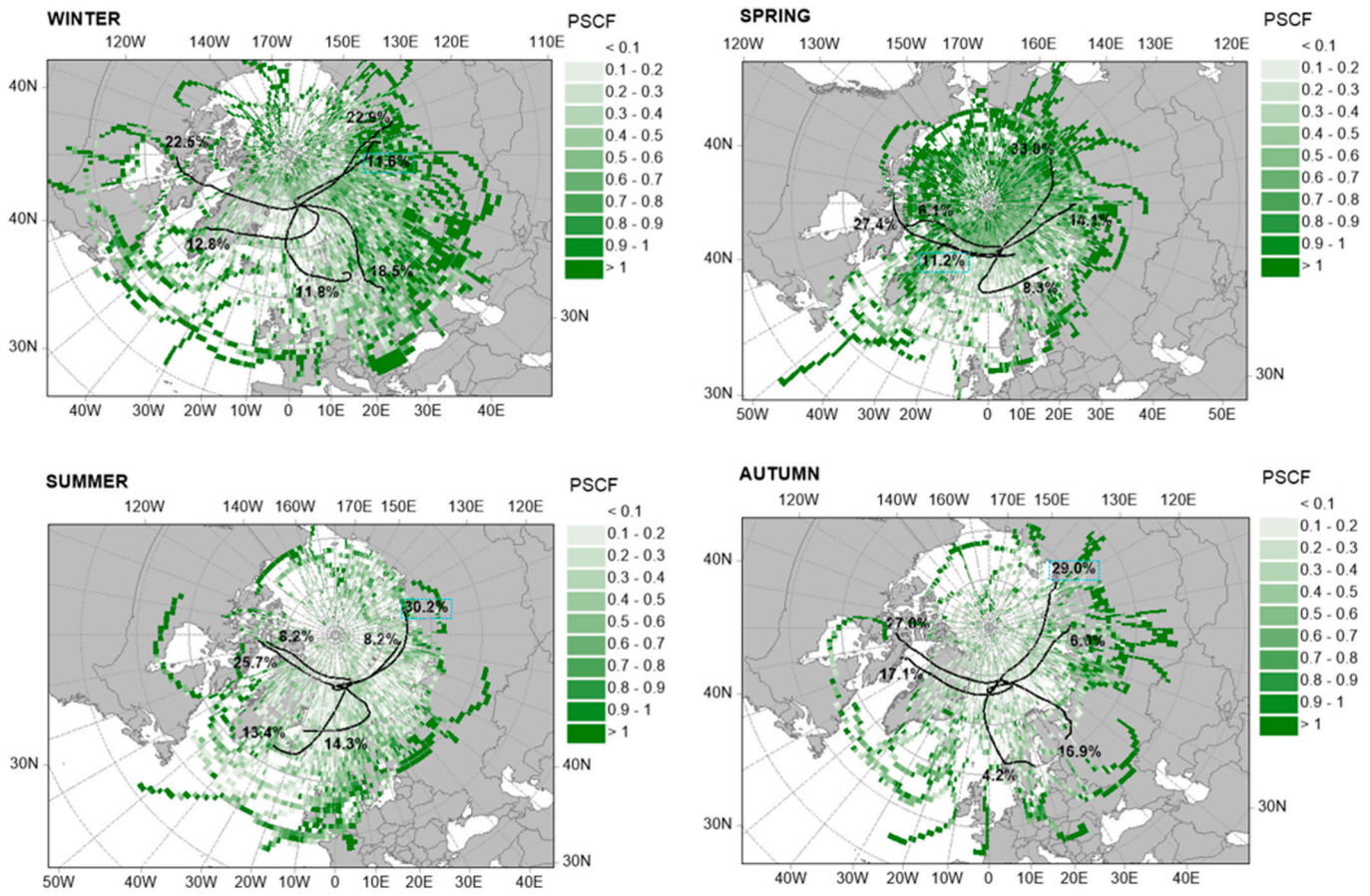


Fig. 13. PSCF plots for BC mass concentrations at different periods of winter, spring, summer, and autumn.

Wm^{-2} at the surface with corresponding TOA forcing of 0.15–2.69 Wm^{-2}.

8. Potential source contribution function revealed the dominant source areas over Europe and Russia in contributing to the high BC mass concentrations during winter and spring.

Declaration of competing interest

The authors declare that they have no known competing financial interests or personal relationships that could have appeared to influence the work reported in this paper.

Acknowledgment

This work was carried out as part of Indian Scientific Expeditions to the Arctic, conducted by the National Centre for Polar and Ocean Research (NCPOR), Goa. We offer our sincere thanks to Director, NCPOR, and Dr. K. P. Krishnan and his team for arranging the expeditions and helping us in the infrastructure development for conducting scientific experiments in the Arctic. The experiment was supported by the Aerosol Radiative Forcing over India (ARFI) project of ISRO GBP. We acknowledge the kind support of Dr. Thamban Meloth, NCPOR for providing the analytical facilities for carrying out ionic analysis of aerosol samples. The help of Ashish Painginkar, NCPOR is humbly acknowledged throughout the IC analysis.

Appendix A. Supplementary data

Supplementary data to this article can be found online at https://doi.org/10.1016/j.polar.2021.100700.

References

Anderson, T.L., Covert, D.S., Marshall, S.F., Laucks, M.L., Charlson, R.J., Waggoner, A.P., Ogren, J.A., Caldow, R., Holm, R.L., Quant, F.R., Sem, G.J., Wiedensohler, A., Ahlquist, N.A., Bates, 1996. Performance characteristics of a high-sensitivity, three-wavelength, total scatter/backscatter nephelometer. J. Atmos. Ocean Tech. 13 (5), 967–986. https://doi.org/10.1175/1520-0426(1996)013<0967:PCOAHS>2.0.CO;2.

Andrews, E., Sheridan, P.J., Fiebig, M., McComiskey, A., Ogren, J.A., Arnott, P., Covert, D., Elleman, R., Gasparini, R., Collins, D., Jonsson, H., Schmid, B., Wang, J., 2006. Comparison of methods for deriving aerosol asymmetry parameter. J. Geophys. Res. 111, D05S04. https://doi.org/10.1029/2004JD005734.

Arun, B.S., Aswini, A.R., Gogoi, M.M., Hegde, P., Kompalli, S.K., Sharma, P.S., Babu, S.S., 2019. Physico-chemical and optical properties of aerosols at a background site (~ 4 km a.s.l.) in the western Himalayas. Atmos. Environ. 218, 117017. https://doi.org/10.1016/j.atmosenv.2019.117017.

Barrett, T.E., Sheesley, R.J., 2017. Year-round optical properties and source characterization of Arctic organic carbon aerosols on the North Slope Alaska. J. Geophys. Res. https://doi.org/10.1002/2016JD026194.

Barrie, L.A., 1986. Arctic Air Pollution: an overview of current knowledge. Atmos. Environ. 20, 643–663.

Barrie, L.A., Hoff, R.M., 1985. Five years of air chemistry, observations in the Canadian Arctic. Atmos. Environ. 19, 1995–2010.

Behera, S.N., Balasubramanian, R., 2014. Influence of biomass burning on temporal and diurnal variations of acidic gases, particulate nitrate, and sulfate in a tropical urban atmosphere. Adv. Meteorol. https://doi.org/10.1155/2014/828491.

Beine, H.J., Argentini, S., Maurizi, A., Mastrantonio, G., Viola, A., 2001. The local wind field at Ny-Ålesund and the Zeppelin mountain at Svalbard. Meteorol. Atmos. Phys. 78, 107–113.

Bodhaine, B.A., 1995. Aerosol absorption measurements at Barrow, mauna loa and the south pole. J. Geophys. Res. 100, 8967–8976. https://doi.org/10.1029/95JD00513.

Bowen, H.J.M., 1979. Environmental Chemistry of the Elements. Elsevier, New York.

Breider, T.J., Mickley, L.J., Jacob, D.J., Wang, Q., Fisher, J.A., Chang, R.Y.-W., Alexander, B., 2014. Annual distributions and sources of Arctic aerosol components, aerosol optical depth, and aerosol absorption. J. Geophys. Res. Atmos. 119, 4107–4124. https://doi.org/10.1002/2013JD020996.

Breider, T.J., Mickley, Loretta J., Jacob, D.J., Ge, C., Wang, J., Sulprizio, M.P., Croft, B., Ridley, D.A., McConnell, J.R., Sharma, S., Husain, L., Dutkiewicz, V.A., Eleftheriadis, K., Skov, H., Hopke, P.K., 2017. Multi decadal trends in aerosol radiative forcing over the Arctic: contribution of changes in anthropogenic aerosol to

Arctic warming since 1980. J. Geophys. Res. Atmos. 122, 3573–3594. https://doi.org/10.1002/2016JD025321.
Bray, C.D., Battye, W., Aneja, V.P., Tong, D.Q., Lee, P., Tang, Y., 2018. Ammonia emissions from biomass burning in the continental United States. Atmos. Environ. 187, 50–61.
Brock, C.A., Cozic, J., Bahreini, R., FroydK, D., Middlebrook, A.M., et al., 2011. Characteristics, sources,and transport of aerosols measured in spring 2008 during the aerosol, radiation, and cloud processes affecting arctic climate (ARCPAC) project. Atmos. Chem. Phys. 11, 2423–2453. https://doi.org/10.5194/acp-11-2423-2011.
Chaubey, J.P., Moorthy, K.K., Babu, S.S., Nair, V.S., Tiwari, A., 2010. Black Carbon aerosols over coastal Antarctica and its scavenging by snow during the Southern Hemispheric summer. J. Geophys. Res. Atmos. 115 (D10), 210. https://doi.org/10.1029/2009JD013381.
Deshpande, C.G., Kamra, A.K., 2014. Physical properties of the arctic summer aerosol particles in relation to sources at Ny-Alesund. Svalbard, J. Earth Syst. Sci. 123 (1), 201–212.
Draxler, R.R., Hess, G.D., 1998. Description of the hysplit 4 modelling system, NOAA tech. Memo. ERL ARL-224. In: Natl. Oceanic and Atmos. Admin (Washington, D.C).
Eleftheriadis, K., Vratolis, S., Nyeki, S., 2009. Aerosol black carbon in the European arctic: measurements at Zeppelin station, ny-ålesund, svalbard from 1998–2007. Geophys. Res. Lett. 36, L02809. https://doi.org/10.1029/2008GL035741.
Feng, Y., Ramanathan, V., Kotamarthi, V.R., 2013. Brown carbon: a significant atmospheric absorber of solar radiation? Atmos. Chem. Phys. 13, 8607–8621. https://doi.org/10.5194/acp-13-8607-2013.
Ferek, R.J., Hobbs, P.V., Radke, L.J., Herring, H.A., Sturges, W.T., Cota, G.J., 1995. Dimethyl sulfide in the arctic atmosphere. J. Geophys. Res. 100, 26,093–26,104.
Flanner, M.G., etal, 2007. Present day climate forcing and response from black carbon in snow. J. Geophys. Res. 112, D11202. https://doi.org/10.1029/2006JD008003.
Flanner, M.G., Zender, C.S., Hess, P.G., Mahowald, N.M., Painter, T.H., Ramanathan, V., Rasch, P.J., 2009. Spring time warming and reduced snow cover from carbonaceous particles. Atmos. Chem. Phys. 9, 2481–2497.
Garrett, T.J., Brattström, S., Sharma, S., Worthy, D.E.J., Novelli, P., 2011. The role of scavenging in the seasonal transport of black carbon and sulfate to the Arctic. Geophys. Res. Lett. 38, L16805. https://doi.org/10.1029/2011GL048221.
Giardi, F., Becagli, S., Traversi, R., Frosini, D., Severi, M., Caiazzo, L., Ancillotti, C., Cappelletti, D., Moroni, B., Grotti, M., Bazzano, A., Lupi, A., Mazzola, M., Vitale, V., Abollino, O., Ferrero, L., Bolzacchini, E., Viola, A., Udisti, R., 2016. Size distribution and ion composition of aerosol collected at Ny-Ålesund in the spring-summer field campaign 2013. Rend. Fis. Acc. Lincei. https://doi.org/10.1007/s12210-016-0529-3.
Gilardoni, S., Lupi, A., Mazzola, M., Cappelletti, D., Moroni, B., Luca, Ferrero, Markuszewski, P., Rozwadowska, A., Krejci, R., Zieger, P., Tunved, P., Linn, Karlsson Vratolis, S., Eleftheriadis, K., Viola, A., 2019. Atmospheric Black Carbon in Svalbard (ABC Svalbard), SESS Report 2019.
Gogoi, M.M., Pathak, B., Moorthy, K.K., Bhuyan, P.K., Babu, S.S., Bhuyan, K., Kalita, G., 2011. Multi-year investigations of near-surface and columnar aerosols over Dibrugarh, Northeastern location of India: heterogeneity in source impacts. Atmos. Environ. 45, 1714–1724. https://doi.org/10.1016/j.atmosenv.2010.12.056.
Gogoi, M.M., Moorthy, K.K., Kompalli, S.K., Chaubey, J.P., Babu, S.S., Manoj, M.R., Nair, V.S., Prabhu, T.P., 2014. Physical and optical properties of aerosols in a free tropospheric environment: results from long-term observations over western trans-Himalayas. Atmos. Environ. 84, 262–274. https://doi.org/10.1016/j.atmosenv.2013.11.029.
Gogoi, M.M., Babu, S.S., Pandey, S.K., Nair, V.S., Vaishya, A., Girach, I.A., Koushik, N., 2018. Scavenging ratio of black carbon in the Arctic and the Antarctic. Polar Science 16, 10–22. https://doi.org/10.1016/j.polar.2018.03.002.
Gogoi, M.M., Babu, S.S., Moorthy, K.K., Thakur, R.C., Chaubey, J.P., Nair, V.S., 2016. Aerosol black carbon over Svalbard regions of Arctic. Pol. Sci. 10.10.1016/j.polar.2015.11.001.
Gogoi, M.M., Babu, S.S., Arun, B.S., et al., 2021. Response of ambient BC concentration across the Indian region to the nation-wide lockdown: results from the ARFINET measurements of ISRO-GBP. Curr. Sci. 120 (2), 341–351. https://doi.org/10.18520/cs/v120/i2/341-351.
Hansen, J., Nazarenko, L., 2004. Soot climate forcing via snow and ice albedos. Proc. Natl. Acad. Sci. U.S.A. 97–101, 423–428. https://doi.org/10.1073/pnas.2237157100, 10-1073-pnas-2237157100.
Hansen, J., Sato, M., Ruedy, R., Lacis, A., Oinas, V., 2000. Global warming in the twenty-first century: an alternative scenario. Proc. Natl. Acad. Sci. Unit. States Am. https://doi.org/10.1073/pnas.170278997.
Hegg, D.A., Clarke, A.D., Doherty, S.J., Strom, J., 2011. Measurements of black carbon aerosol washout ratio on Svalbard. Tellus B 63 (5), 891–900.
Heidam, N.Z., Christensen, J., Wåhlin, P., Skov, H., 2004. Arctic atmospheric contaminants in NE Greenland: levels,variations, origins, transport, transformations and trends 1990–2001. Sci. Total Environ. 331, 5–28.
Hyvarinen, A.-P., Lihavainen, H., Komppula, M., Sharma, V.P., Kerminen, V.-M., Panwar, T.S., Viisanen, Y., 2009. Continuous measurements of optical properties of atmospheric aerosols in Mukteshwar, northern India. J. Geophys. Res. 114 (D8), D08207. https://doi.org/10.1029/2008JD011489.
IPCC, 2013. In: Stocker, T.F., Qin, D., Plattner, G.-K., Tignor, M., Allen, S.K., Boschung, J., Nauels, A., Xia, Y., Bex, V., Midgley, P.M. (Eds.), The Physical Science Basis. Contribution of Working Group I to the Fifth Assessment Report of the Intergovernmental Panel on Climate Change. Cambridge Univ. Press, Cambridge, UK andNew York, NY, USA.
IPCC, 2018. Summary for policymakers. In: Global Warming of 1.5°C.
Iziomon, M.G., Lohmann, U., Quinn, P.K., 2006. Summer time pollution events in the Arctic and potential Implications. J. Geophys. Res. 111, D12206. https://doi.org/10.1029/2005JD006223.
Jacobson, J.Z., 2004. Climate response of fossil fuel and biofuel soot, accounting for soot's feedback to snow and sea ice albedo and emissivity. J. Geophys. Res. 109, D21201. https://doi.org/10.1029/2004JD004945.
Kodros, J.K., Hanna, S.J., Bertram, A.K., Leaitch, W.R., Schulz, H., Herber, A.B., Zanatta, M., Burkart, J., Willis, M.D., Abbatt, J.P.D., Pierce, J.R., 2018. Size-resolved mixing state of black carbon in the Canadian high Arctic and implications for simulated direct radiative effect. Atmos. Chem. Phys. 18, 11345–11361. https://doi.org/10.5194/acp-18-11345-2018.
Leck, C., Persson, C., 1996. Seasonal and short-term variability in dimethyl Sulphide, sulfur dioxide and biogenic sulfur and sea salt aerosol particles in the arctic marine boundary layer during summer and autumn. Tellus B 48 (2), 272–299. https://doi.org/10.3402/tellusb.v48i2.15891.
Lefohn, A.S., Husar, J.D., Husar, R.B., 1999. Estimating historical anthropogenic global sulfur emission patterns for the period 1850–1990. Atmos. Environ. 33 (21), 3435–3444. https://doi.org/10.1016/S1352-2310(99)00112-0.
Lisok, J., Rozwadowska, A., Pedersen, J.G., Markowicz, K.M., Ritter, C., Kaminski, J.W., et al., 2018. Radiative impact of an extreme Arctic biomass-burning event. Atmos. Chem. Phys. 18 (12), 8829–8848. https://doi.org/10.5194/acp-18-8829-2018.
Manktelow, P.T., Mann, G.W., Carslaw, K.S., Spracklen, D.V., Chipperfield, M.P., 2007. Regional and global trends in sulfate aerosol since the 1980s. Geophys. Res. Lett. 34, L14803. https://doi.org/10.1029/2006GL028668.
Marinoni, A., Cristofanelli, P., Laj, P., Duchi, R., Calzolari, F., Decesari, S., Sellegri, K., Vuillermoz, E., Verza, G.P., Villani, P., Bonasoni, P., 2010. Aerosol mass and black carbon concentrations, a two-year record at NCO-P (5079 m, Southern Himalayas). Atmos. Chem. Phys. 10 (17), 8551–8562. https://doi.org/10.5194/acp-10-8551-2010.
Markowicz, K.M., Manko, O.Z., Lisok, J., Chilinski, M.T., Xian, P., 2021. The impact of moderately absorbing aerosol on surface sensible, latent, and net radiative fluxes during the summer of 2015 in Central Europe. J. Aerosol Sci. 151, 105627. https://doi.org/10.1016/j.jaerosci.2020.105627.
Markowicz, K.M., Pakszys, P., Ritter, C., Zielinski, T., Udisti, R., Cappelletti, D., et al., 2016. Impact of North American intense fires on aerosol optical properties measured over the European Arctic in July 2015. Geophys. Res: Atmosphere 121, 14. https://doi.org/10.1002/2016JD025310, 487–14,512.
Moroni, B., Becagli, S., Bolzacchini, E., Busetto, M., Cappelletti, D., Crocchianti, S., Ferrero, L., Frosini, D., Lanconelli, C., Lupi, A., Maturilli, M., Mazzola, M., Perrone, M.G., Sangiorgi, G., Traversi, R., Udisti, R., Viola, A., Vitale, V., 2015. Vertical profiles and chemical properties of aerosol particles upon Ny-Ålesund (Svalbard Islands). Adv. Meteorol. https://doi.org/10.1155/2015/292081, 2015.
Morys, M., Mims, F.M., Hagerup, S., Anderson, S.E., Baker, A., Kia, J., Walkup, T., 2001. Design, calibration, and performance of MICROTOPS II handheld ozone monitor and Sun photometer. J. Geophys. Res. 106 (D13), 14573–14582.
Moroni, B., Cappelletti, D., Crocchianti, S., Becagli, S., Caiazzo, L., Traversi, R., Udisti, R., Mazzola, M., Markowicz, K., Ritter, C., Zielinski, T., 2017. Morphochemical characteristics and mixing state of long range transported wildfire particles at Ny-Ålesund (Svalbard Islands). Atmos. Environ. 156, 135–145. https://doi.org/10.1016/j.atmosenv.2017.02.037.
Nagel, D., Herber, A., 1998. Vertical distribution of the spectral aerosoloptical depthinthe arctic from 1993 to 1996. J. Geophys. Res. 103, 1857–1870. https://doi.org/10.1029/97JD02678.
Nair, Vs S., Jayachandran, V., Kompalli, S.K., Gogoi, M.M., Babu, S.S., 2020. Cloud condensation nuclei properties of south asian outflow over the northern Indian ocean during winter. Atmos. Chem. Phys. 20, 3135–3149. https://doi.org/10.5194/acp-20-3135-2020.
Nikonovas, T., North, P.R.J., Doerr, S.H., 2016. Particulate emissions from large North American wildfires estimated using a new top-down method. Atmos. Chem. Phys. 17, 6423–6438. https://doi.org/10.5194/acp-2016-277.
Nozaki, Y., 1997. A fresh look at element distribution in the North Pacific Ocean, Eos. transactions American Geophysical Union 78 (21). https://doi.org/10.1029/97EO00148, 221–221.
Nyeki, S., Coulson, G., Colbeck, I., Eleftheriadis, K., Baltensperger, U., Beine, H.J., 2005. Overview of aerosol microphysics at arctic sunrise: measurements during the NICE renoxification study. Tellus, Ser. B 57, 40–50.
Pakszys, P., Zielinski, T., 2017. Aerosol optical properties over svalbard: a Comparison between ny-ålesund and hornsund. Oceanologia 59, 431–444. https://doi.org/10.1016/j.oceano.2017.05.002.
Pillai, P.S., Moorthy, K.K., 2001. Aerosol mass-size distributions at a tropical coastal environment: response to mesoscale and synoptic processes. Atmos. Environ. https://doi.org/10.1016/S1352-2310(01)00211-4.
Quinn, P.K., Shaw, G., Andrews, E., Dutton, E.G., Airola, T.R., Gong, S.L., 2007. Arctic haze: current trends and knowledge gaps. Tellus, Ser. B 59 (1), 99–114. https://doi.org/10.1111/j.1600-0889.2006.00238.
Radke, L.F., hobbs, P.V., Bailey, I.H., 1984. Airborn eobservations of Arctic aerosols, III: origins and effects of air masses. Geophys. Res. Lett. 11, 401–404.
Ren, L., Yang, Y., Wang, H., Zhang, R., Wang, P., Liao, H., 2020. Source attribution of Arctic black carbon and sulfate aerosols and associated Arctic surface warming during 1980–2018. Atmos. Chem. Phys. https://doi.org/10.5194/acp-20- 9067-2020.
Ricchiazzi, P., Yang, S., Gautier, C., Sowle, D., 1998. SBDART: a research and teaching software tool for plane-parallel radiative transfer in the Earth's atmosphere. Bull. Am. Meteorol. Soc. 79, 2101–2114.
Ritter, C., Angeles Burgos, M., Böckmann, C., Mateos, D., Lisok, J., Markowicz, K.M., et al., 2018. Microphysical properties and radiative impact of an intense biomass

burning aerosol event measured over Ny-Ålesund, Spitsbergen in July 2015. Tellus: Chem. Phys. Meteorol. 70 (1), 1–23. https://doi.org/10.1080/16000889.2018.1539618.

Rongming, H., Planton, S., Deque, M., Marquet, P., Braun, A., 2001. Why is the climate forcing of Sulphate aerosols so uncertain. Adv. Atmos. Sci. 18 (6), 1103–1120. https://doi.org/10.1007/s00376-001-0026-0.

Schmeisser, L., Backman, J., Ogren, A.J., Andrews, E., Asmi, E., Starkweather, S., Uttal, T., Fiebig, M., Sharma, S., Eleftheriadis, K., Vratolis, S., Bergin, M., Tunved, P., Jefferson, A., 2018. Seasonality of aerosol optical properties in the Arctic. Atmos. Chem. Phys. 18, 11599–11622. https://doi.org/10.5194/acp-18-11599-2018.

Sharma, S., Lavoué, D., Cachier, H., Barrie, L.A., 2004. Long-term trends of the black carbon concentrations in the Canadian Arctic. J. Geophys. Res. 109, D15203. https://doi.org/10.1029/2003JD004331.

Shaw, G.E., 1995. The Arctic haze phenomenon. Bull. Am. Meteorol. Soc. 76, 2403–2413.

Shen, Z., Ming, Y., Horowitz, L.W., Ramaswamy, V., Lin, M., 2017. On the seasonality of arctic black carbon. J. Clim. 30, 4429–4441. https://doi.org/10.1175/JCLI-D-16-0580.1, 2017.

Shindell, D.T., Chin, M., Dentener, F., Doherty, R.M., Faluvegi, G., Fiore, A.M., Hess, P., Koch, D.M., MacKenzie, I.A., Sanderson, M.G., Schultz, M.G., Schulz, M., Stevenson, D.S., Teich, H., Textor, C., Wild, O., Bergmann, D.J., Bey, I., Bian, H., Cuvelier, C., Duncan, B.N., Folberth, G., Horowitz, L.W., Jonson, J., Kaminski, J.W., Marmer, E., Park, R., Pringle, K.J., Schroeder, S., Szopa, S., Takemura, T., Zeng, G., Keating, T.J., Zuber, A., 2008. A multi-model assessment of pollution transport to the Arctic. Atmos. Chem. Phys. 8, 5353–5372. https://doi.org/10.5194/acp-8-5353-2008.

Shindell, D.T., 2007. Local and remote contributions to Arctic warming. Geophys. Res. Lett. 34, L14704. https://doi.org/10.1029/2007GL030221.

Stohl, A., Andrews, E., Burkhart, J.F., Forster, C., Herber, A., Hoch, S.W., Kowal, D., Lunder, C., Mefford, T., Ogren, J.A., Sharma, S., Spichtinger, N., Stebel, K., Stone, R., Strom, J., Tørseth, K., Wehrli, C., Yttri, K.E., 2006. Pan-Arctic enhancements of light absorbing aerosol concentrations due to North American boreal forest fires during summer 2004. J. Geophys. Res. 111, D22214.

Struthers, H., Ekman, A.M.L., Glantz, P., Iversen, T., Kirkevag, A., Martensson, E.M., Seland, Ø., Nilsson, E.D., 2010. The effect of sea ice loss on sea salt aerosol concentrations and the radiative balance in the Arctic. Atmos. Chem. Phys. Discuss. 10, 28859–28908. https://doi.org/10.5194/acpd-10-28859-2010, 2010.

Sun, J., Birmili, W., Hermann, M., Tuch, T., Weinhold, K., Merkel, M., Rasch, F., Müller, T., Schladitz, A., Bastian, S., Cyrys, G.L.J., Gu, J., Flentje, H., Briel, B., Asbach, C., Kaminski, H., Ries, L., Sohmer, R., Gerwig, H., Wirtz, K., Meinhardt, F., Schwerin, A., Bath, O., Ma, N., Wiedensohler, A., 2020. Decreasing trends of particle number and black carbon mass concentrations at Observational sites in Germany from 2009 to 2018. Atmos. Chem. Phys. 20, 7049–7068. https://doi.org/10.5194/acp-20-7049-2020, 2020.

Thakur, R.C., Thamban, M., 2019. Influence of gaseous and particulate species on neutralization processes of polar aerosol and snow — a case study from Ny-Ålesund. J. Environ. Sci. 76, 12–25. https://doi.org/10.1016/j.jes.2018.03.002.

Tomasi, C., Vitale, V., Lupi, A., Carmine, C.D., Campanelli, M., Herber, A., Treffeisen, R., Stone, R.S., Andrews, E., Sharma, S., Radionov, V., Huene, W.H., Stebel, K., Hansen, G.H., Myhre, C.L., Wehrli, C., Aaltonen, V., Lihavainen, H., Virkkula, A., Hillamo, R., Stroem, J., Toledano, C., Cachorro, V.E., Ortiz, P., Frutos, A.M., Blindheim, S., Frioud, M., Gausa, M., Zielinski, T., Petelski, T., Yamanouchi, T., 2007. Aerosols in polar regions: a historical overview based on optical depth and in-situ observations. J. Geophys. Res. 112, D16205. https://doi.org/10.1029/2007JD008432.

Tomasi, C., Lupi, A., Mazzola, M., Stone, R.S., Dutton, E.G., Herber, A., Radionov, V.F., Holben, B.N., Sorokin, M.G., Sakerin, S.M., Terpugova, S.A., Sobolewski, P.S., Lanconelli, C., Petkov, B.H., Busetto, M., Vitale, V., 2012. An update on polar aerosol optical properties using POLAR-AOD and other measurements performed during International Polar Year. Atmos. Environ. 52, 9–47. https://doi.org/10.1016/j.atmosenv.2012.02.055.

Udisti, R., Bazzano, A., Becagli, S., Bolzacchini, E., Caiazzo, L., Cappelletti, D., Ferrero, L., Frosini, D., Giardi, F., Grotti, M., Lupi, A., Malandrino, M., Mazzola, M., Moroni, B., Severi, M., Traversi, R., Viola, A., Vitale, V., 2016. Sulfate source apportionment in the ny-ålesund (svalbard islands) arctic aerosol. Rend. Lincei. 27, 85–94. https://doi.org/10.1007/s12210-016-0517-7.

Virkkula, A., Teinila, K., Hillamo, R., Kerminen, V.M., Saarikoski, S., Aurela, M., Viidanoja, J., Paatero, J., Koponen, I.K., Kulmala, M., 2006. Chemical composition of boundary layer aerosol over the Atlantic Ocean and at an Antarctic site. Atmos. Chem. Phys. 6, 3407–3421. https://doi.org/10.1029/2004JD004958.

Wagenbach, D., Preunkert, S., Schafer, J., Jung, W., Tomadin, L., 1996. Northward transport of Saharan dust recorded in a deep alpine ice core. In: Guerzoni, S., Chester, R. (Eds.), The Impact of Desert Dust across the Mediterranean. Env. Sc. Tech. Lib, vol. 11. Springer, The Netherlands, pp. 291–300.

Warneke, C., Bahreini, R., Brioude, J., Brock, C.A., de Gouw, J.A., Fahey, D.W., Froyd, K. D., Holloway, J.S., Middlebrook, A., Miller, L., Montzka, S., Murphy, D.M., Peischl, J., Ryerson, T.B., Schwarz, J.P., Spackman, J.R., Veres, P., 2009. Biomass burning in Siberia and Kazakhstan as an important source for haze over the alaskan arctic in April 2008. Geophys. Res. Lett. 36, L02813. https://doi.org/10.1029/2008GL036194.

Zhan, J., Gao, Y., 2014. Impact of summertime anthropogenic emissions on atmospheric black carbon at Ny-Ålesund in the Arctic. Pollut. Res. 33 (1), 21821. https://doi.org/10.3402/polar.v33.21821.

Zhan, J., Gao, Y., Li, W., Chen, L., Lin, H., Lin, Q., 2014. Effects of ship emissions on summer time aerosols at Ny–Alesund in the Arctic. Atmos. Pol. Res. https://doi.org/10.5094/APR.2014.059.

Zielinski, T., Bolzacchini, E., Cataldi, M., Ferrero, L., Graßl, S., Hansen, G., Mateos, D., Mazzola, M., Neuber, R., Pakszys, P., Posyniak, M., Ritter, C., Severi, M., Sobolewski, P., Traversi, R., Velasco-Merino, C., 2020. Study of chemical and optical properties of biomass burning aerosols during long-range transport events toward the arctic in summer 2017. Atmosphere 11, 84.